

1 Title: Molecular architecture of human dermal sleeping nociceptors

2 Authors:

3 Jannis Körner^{1,2,3,4†}, Derek Howard^{5†}, Hans Jürgen Solinski^{6‡}, Marisol Mancilla Moreno^{7‡}, Natja Haag^{4,8}, Andrea
4 Fiebig^{4,9}, Shamsuddin A. Bhuiyan¹⁰, Idil Toklucu¹, Raya Bott¹, Ishwarya Sankaranarayanan⁷, Diana Tavares-
5 Ferreira⁷, Stephanie Shiers⁷, Nikhil N. Inturi⁷, Anna Maxion^{4,9}, Lisa Ernst¹¹, Lorenzo Bonaguro^{12,13}, Jonas Schulte-
6 Schrepping^{12,13}, Marc D. Beyer^{12,13,14}, Thomas Stiehl^{14,15,16}, William Rental¹⁰, Ingo Kurth^{4,8}, Theodore Price⁷, Martin
7 Schmelz⁶, Barbara Namer^{1,4,9§}, Shreejoy Tripathy^{5,17,§,*}, Angelika Lampert^{1,4,§,*}

8 Affiliations:

9 ¹Institute of Neurophysiology, Uniklinik RWTH Aachen University; Aachen, Germany.

10 ²Department of Anesthesiology, Uniklinik RWTH Aachen University; Aachen, Germany.

11 ³Department of Intensive and Intermediate Care, Uniklinik RWTH Aachen University;
12 Aachen, Germany.

13 ⁴Scientific Center for Neuropathic pain Aachen SCN^{AACHEN}, Uniklinik RWTH Aachen
14 University; Aachen, Germany.

15 ⁵Krembil Centre for Neuroinformatics, Centre for Addiction and Mental Health; Toronto,
16 Ontario, Canada.

17 ⁶Department of Experimental Pain Research, MCTN, Medical Faculty Mannheim;
18 Heidelberg University, Ludolf-Krehl-Strasse 13-17, 68167, Mannheim, Germany.

19 ⁷The Department of Neuroscience, The University of Texas at Dallas; 800 West Campbell
20 RD, Richardson TX 75080, USA.

21 ⁸Institute for Human Genetics and Genomic Medicine, Uniklinik RWTH Aachen University;
22 Aachen, Germany.

23 ⁹Research Group Neuroscience, Interdisciplinary Center for Clinical Research within the
24 Faculty of Medicine at the RWTH Aachen University; Aachen, Germany.

25 ¹⁰Department of Neurology, Brigham and Women's Hospital and Harvard Medical School,
26 Boston, MA 02115, USA.

27 ¹¹Institute for Laboratory Animal Science and Experimental Surgery, Uniklinik RWTH
28 Aachen University; Aachen, Germany.

29 ¹²PRECISE Platform for Single Cell Genomics and Epigenomics at DZNE & University of
30 Bonn and West German Genome Center; Bonn, Germany.

31 ¹³Systems Medicine, Deutsches Zentrum für Neurodegenerative Erkrankungen (DZNE);
32 Bonn, Germany.

33 ¹⁴Immunogenomics & Neurodegeneration, Deutsches Zentrum für Neurodegenerative
34 Erkrankungen (DZNE); Bonn, Germany.

35 ¹⁵Joint Research Center for Computational Biomedicine (JRCC), Pauwelsstrasse 30, 52074
36 Aachen, Germany

37 ¹⁶Institute for Computational Biomedicine and Disease modelling with focus on phase
38 transitions between phenotypes, Pauwelsstrasse 30, 52074 Aachen, Germany

39 ¹⁷Department of Psychiatry, University of Toronto; Toronto, Ontario, Canada.

40 †, ‡, § These authors contributed equally

41 *Corresponding author. Email alampert@ukaachen.de ; shreejoy.tripathy@camh.ca

42 **One Sentence Summary:** We identify the molecular architecture and specifically OSMR and
43 SST as molecular markers for human dermal sleeping nociceptors, key players in the generation
44 of neuropathic pain.

45 **Short version:** In this Patch-seq study, we identify OSMR and SST as molecular markers for
46 human dermal sleeping nociceptors, key players in the generation of neuropathic pain.

47 **Abstract:**

48 Human dermal sleeping nociceptors display ongoing activity in neuropathic pain, affecting 10%
49 of the population. Despite advances in rodents, a molecular marker for these mechano-insensitive
50 C-fibers (CMis) in human skin remains elusive, preventing targeted therapy. In this translational
51 Patch-seq study, we combine single-cell transcriptomics following electrophysiological
52 characterization with single-nucleus and spatial transcriptomics from pigs and humans. We
53 functionally identified CMis in pig sensory neurons with patch-clamp using adapted protocols
54 from human microneurography. We identified oncostatin-M-receptor (OSMR) and somatostatin
55 (SST) as marker genes for CMis. Following dermal injection in healthy human volunteers,
56 oncostatin-M, the ligand of OSMR, exclusively modulates CMis. We identified the entire
57 molecular architecture of human dermal sleeping nociceptors, providing new therapeutic targets
58 and the basis for a mechanistic understanding of neuropathic pain.

59

60 **Main Text:**

61 **INTRODUCTION**

62 Neuropathic pain, which affects 10% of the population and 20-30% of diabetic patients,
63 correlates with increased activity of sensory neurons in the skin called by the fairly misleading
64 name “sleeping” or “silent” nociceptors (1–5). They are defined in human microneurography and
65 psychophysics studies of the skin as mechano-insensitive C-fibers (CMi-fibers (6), also termed
66 type 1b fibers (7)), and show pronounced chemical responsiveness, e.g. to capsaicin, ATP, partly
67 to histamine, and several inflammatory mediators (8–11). Under inflammatory and other painful
68 conditions, CMi-fibers can be sensitized to mechanical stimuli, becoming similar to polymodal
69 nociceptors (CM-fibers or type 1a-fibers (12)).

70 Human skin contains CMis that can be reliably identified by their distinct functional and
71 biophysical properties (13–16). In contrast, rodents lack these homologous neurons in their skin;
72 instead, similar neurons primarily innervate internal organs (17). The few mechano-insensitive
73 C-fibers identified in rodent skin display significantly different biophysical properties compared
74 to human CMis (18, 19). While rodent models crucially advance our understanding, they limit
75 our ability to deduce molecular markers or new drug targets relevant for human skin sleeping
76 nociceptors (20). In contrast, pig skin is innervated by neurons resembling human CMis showing
77 tight correlations among mechanical, chemical and biophysical properties (21, 22). This
78 similarity provides a valuable translational model for studying dermal nociceptive fibers relevant
79 for human neuropathic pain. In mice, mechano-sensitivity appears less tightly correlated to
80 biophysical properties than in human and pigs, and the functional roles of chemosensing and
81 disease-related hyperactivity may be assumed by other nociceptor classes (23).

82 CMi-fibers are insensitive to strong mechanical stimulation unless sensitized and are unable to
83 follow high-frequency electrical pulses, even when sensitized (16). These fibers preferentially
84 respond to slow depolarization, such as low frequency sinusoidal pulses rather than square pulses
85 (13). A characteristic feature of these fibers is their enhanced activity-dependent slowing (ADS)
86 upon repetitive stimulation: when stimulated electrically with 2 Hz pulses in the receptive field
87 for an extended time, the conduction velocity of action potentials (APs) traveling along the nerve
88 fiber is reduced (22). The distinct electrophysiological characteristics of CMis likely stem from
89 their unique molecular architecture (24), potentially offering an opportunity to identify specific,
90 conserved markers for human CMis. In this study, we characterize the molecular architecture of
91 these nociceptors in pigs and humans identifying oncostatin-M receptor (OSMR) and
92 somatostatin (SST) as marker genes for CMis.

93
94
95
96

97 **RESULTS**

98 **An integrated multi-modal taxonomy for pig peripheral sensory neurons**

99 Single cell transcriptomic studies of peripheral sensory neurons have revealed a molecular
100 taxonomy of highly specialized and diverse cells responsible for various aspects of sensory
101 perception like pain (25–30). In contrast, functional single cell in vitro patch-clamp studies have
102 not yielded a similarly comprehensive cellular taxonomy based on sensory neuron excitability,
103 especially of large mammals given their described difference in electrophysiology compared to
104 rodents (31). Recent Patch-seq techniques, however, provide a unique opportunity for bridging
105 the molecular identities of dorsal root ganglion (DRG) neurons with their electrophysiological
106 and morphological identity (32–37): individual neurons are electrically characterized via patch-
107 clamp, followed by single cell RNA sequencing.

108 We used Patch-seq to characterize electrophysiological and transcriptomic characteristics of pig
109 DRG neurons, intentionally targeting smaller, likely C-fiber neurons. We assessed up to 27
110 electrophysiological features per cell and visualized cellular morphologies prior to capturing
111 whole-cell mRNA (Fig. S1). We successfully sampled 288 neurons using our improved
112 harvesting protocol (Fig. S2, methods) and analyzed their transcriptome by Smart-seq2 and deep
113 sequencing. Of these, 226 neurons passed rigorous quality control of transcriptomes, with a
114 median of 700,000 reads and 11,000 unique detected genes per cell (Fig. S3), demonstrating the
115 deep transcriptomic characterization provided by this methodology.

116
117 We next applied droplet-based snRNAseq using the 10XGenomics Chromium v3 platform to
118 sample transcriptomes from 16,997 nuclei from flash-frozen pig DRGs. Following rigorous
119 transcriptomic filtering, we obtained 2,176 DRG neuronal nuclei, with a median of 4,574
120 detected Unique Molecular Identifiers (UMIs) and 2,131 genes expressed per nucleus. Following
121 unsupervised clustering of snRNAseq-based transcriptomes we identified 16 DRG neuronal
122 subtypes based on distinct marker gene expression (Fig. 1A, see methods). Important pain-
123 related genes, such as *CALCB*, or the receptor for oncostatin M (*OSMR*) were reliably quantified,
124 while a few, including *SCN10A* and *TRPV1*, suffered from some degree of genome annotation
125 incompleteness in the pig, as described previously (Fig. S4, (38)). Despite this, *TRPV1*
126 expression was detected in expected neuronal subtypes (Fig. S5), ensuring that these genome
127 annotation limitations did not impede our ability to identify its presence where anticipated.
128

129
130 We mapped each Patch-seq characterized cell to our larger snRNAseq atlas by gene expression
131 guided integration of the two datasets (Fig. 1A, see methods). Each transcriptomically defined
132 sensory neuron subtype was represented by at least one and up to 74 Patch-seq characterized
133 neurons (Fig. 1B). The integration of snRNAseq and Patch-seq datasets effectively mitigated
134 technical differences between the two approaches, as evidenced by the uniform distribution of cells
135 from different batches and biological replicates across the integrated UMAP space (Fig. S6). While
136 we observed some expected differences in injury-induced and culturing-related genes between the
137 datasets (39, 40) (Fig. S7), cell-type enriched marker genes were largely consistent between either
138 technology (Fig. S8). Patch-seq cells which are mapped to the same molecular cell type display
139 similar electrophysiological properties (Fig. S1). To corroborate our findings, we also performed
140 “spot-based” spatial transcriptomics (Visium technique) from pig DRG neurons (Fig. S9), using

141 the same approach as reported before for human DRG neurons (29), with identification of 5,577
142 putative neurons with a median of 4,597 detected UMIs and 2,138 expressed genes per spot (Fig.
143 S10). Our thorough taxonomy reflects all major expected neuronal DRG populations, consisting
144 of five A β -, four A δ -, and seven C-fiber related neuronal subtypes (Fig. 1, supplement table 1). In
145 naming the cell types in this study, we designated putative fiber types based on gene expression
146 patterns, knowledge on fiber function in large mammals and through comparisons with existing
147 transcriptomic datasets from large mammals, such as humans and monkeys (26, 27, 29). With our
148 approach, we were able to map distinct electrophysiological and morphological features to the
149 transcriptomic identities of the sensory neurons (Fig. 1C, Fig. S1 and S9), e.g. the groups related
150 to C-fibers compared to A-fibers exhibited significantly longer action potential (AP) durations
151 (Fig. 1D) and as expected, had smaller mean diameter cell bodies (Fig. S9).

152
153 The A β -group of putative proprioceptors, A β -Proprio, displayed high expression of *PVALB*,
154 *SPP1* and *ETV1*, hyperpolarized after-hyperpolarization (AHP) minimum (-81.6 ± 1.22 mV) and
155 hyperpolarized AP thresholds (-55.2 ± 4.31 mV) and large cell diameters (95 ± 3.1 μm) (Fig. 1F
156 and Fig. S1, S9). We identified three low-threshold mechanoreceptor subtypes (A β -LTMRs),
157 termed A β -LTMR-ALDH1A1, A β -LTMR-SLIT2, and A β -LTMR-PALM, each expressing
158 *PIEZO2* and showing low expression of the pain related sodium channel genes *SCN9A*, *SCN10A*
159 and *SCN11A*. The A β -fiber neuron group named A β -HTMRs likely represent high-threshold
160 mechanoreceptors, marked by *CPNE4* and *PLXNA2*, as well as *PIEZO2*, and *SCN10A*,
161 suggestive of a potential nociceptive function (29).

162
163 We identified four A δ groups: the A δ -LTMR, with uniquely high expression of *PIEZO2* and
164 marked by *PCDH7*, *KCNQ3*, *NTRK2*; the A δ -CACNA1E, marked by *B4GALT6*, *DCC*, *CREB5*,
165 *CACNA1E*, and - unique among A-fibers - by its relatively high expression of *SCN10A*; the A δ -
166 TRPV1, marked by *UNC5D* and *ZNF521*, and with distinctively high expression of the capsaicin
167 and heat receptor *TRPV1*. The A δ -COOL group was marked by the cold and menthol sensitive
168 ion channel *TRPM8*, *RORA* and *FOXP2* expression. They displayed a very short AP duration
169 (2.01 ± 0.286 ms, Fig. 1D), low AP amplitudes (97.5 ± 2.31 mV) and the highest fraction among
170 all DRG cell types for ongoing activity (61.5%, Fig. S1), potentially due to patch clamp being
171 performed at room temperature which represents a tonic cold stimulus for those cells.

172
173 The C-fiber related groups all displayed high expression of the pain-related sodium channel
174 genes *SCN9A*, *SCN10A* and *SCN11A*. C-COLD, was marked by *TRPM8* and *KIT* and showed
175 moderate *PIEZO2* expression, suggesting potential mechano-sensitivity. We identified three C-
176 fiber related subtypes with high expression of *TAC1*, encoding for the nociception-related
177 neurotransmitter substance P, and each subtype showed APs with large amplitudes (Fig. S1).
178 These three populations differed by strong expression of the potassium channel *KCNQ5* (C-
179 TAC1-KCNQ5), the low-density lipoprotein receptor-related protein 1B (*LRP1B*; C-TAC1-
180 LRP1B), and the pain relevant transient receptor potential channel *TRPA1* (C-TAC1-TRPA1).
181 One C-fiber subtype was marked by *CDH9* and displayed high expression of *PIEZO2* and
182 *GFRA2*; we termed these cells C-LTMRs, given expression of similar markers in a putative
183 orthologous DRG cell type described in humans and mice previously (29, 30). We identified an
184 additional group of C-fibers, termed C-OSMR-GFRA1/2, expressing the receptor for oncostatin-
185 M (OSMR) and marked by expression of *GFRA1*, *GFRA2*, *SYNPR*, and *TMC3*, and with high

186 *PIEZ02* expression, suggestive of potential mechano-sensitivity. Finally, we identified a distinct
187 C-fiber subgroup, notable for its high expression of *OSMR*, low expression of *PIEZ02*, and
188 marked by *IL31RA*, *HRH1* (the histamine receptor), *JAK1*, and *NPPB*. We named this subgroup
189 C-OSMR-SST, given the prominent expression of *SST* among these cells, especially among our
190 whole-cell datasets of these neurons (i.e., Patch-seq and spatial transcriptomics, Fig. 1E, Fig.
191 S11). Notably, these cells expressed the highest levels of *SCN1A* and displayed the longest AP
192 duration of any DRG cell type in our dataset (Fig. 1D).

193

194 In summary, our pig DRG neuronal taxonomy displays marked neuronal diversity in
195 transcriptomic and electrophysiological characteristics.

196 Comparison of pig DRG transcriptomes to cross-species atlases (including human)

197 Transcriptomic studies of sensory neurons have shown evolutionary conservation of major cell
198 identities between species (25, 41). Consequently, to contextualize our pig DRG cell type
199 taxonomy in relation to homologous cell types defined in other species, including humans, we
200 compared the transcriptional identities from our pig snRNAseq dataset with a recently published
201 cross-species atlas of the mammalian DRG (Fig. 2A)(41). Following the projection of our pig
202 snRNAseq dataset onto this atlas (see Methods), we observed a good representation of pig
203 neuronal nuclei among the cell type clusters defined in this broader cross-species atlas (Fig. 2B,
204 2C).

205 To quantify the comparability between the pig and cross-species DRG taxonomies, we employed
206 two complementary analytical approaches. First, we used a Seurat-based label transfer method to
207 project the cross-species atlas cell type labels onto our pig snRNA-seq data. This approach
208 predicts cell type labels for query cells based on transcriptional similarities to the reference
209 dataset. We visualized these results using a river plot (Fig. 2D), which illustrates the flow of cell
210 type assignments from the cross-species classification to our original pig taxonomy. Second, we
211 applied the MetaNeighbor algorithm (39) to evaluate the replicability of cell types across
212 taxonomies. This method quantifies the similarity of cell types based on shared gene expression
213 patterns. We represented these MetaNeighbor scores using a clustergraph plot (Fig. 2E), where
214 edge weights indicate the strength of cell type similarity across taxonomies. For each pig cell
215 type, the top corresponding cell type in the cross-species atlas and its MetaNeighbor area under
216 the curve (AUC) score are provided in Supplementary Table 1.

217 Overall, we observed excellent concordance between cell type nomenclatures, with several
218 examples of strong one-to-one orthologous relationships (delineated in Supplement table 1), such
219 as between *Sst* (cross-species) and C-OSMR-SST (pig), Mrgprd and C-OSMR-GFRA1/2, Th and
220 C-LTMR, and Adelta-COOL and Trmp8, among others. Additionally, we identified a few one-
221 to-many relationships; for instance, the cell type classified as *Pvalb* within the cross-species atlas
222 corresponded to two cell types in our pig taxonomy, A β -PROPRIO and A β -LTMR-SLIT2. We
223 also noted that certain cell types, such as Mrgpra3+Mrgprb4 and Mrgpra3+Trpv1, defined in the
224 cross-species atlas largely based on their prevalence in rodents were less frequent in our pig
225 dataset, suggesting that they may be underrepresented in larger mammals like pigs and humans.

226 While cross-species comparisons offer broad evolutionary insights, they may not fully capture
227 the nuances of larger mammalian systems, particularly for pain-relevant neuronal populations.
228 For instance, the neurons called CMi as characterized by a tight link between lack of
229 mechanosensitivity and specific biophysical properties in human and pig are absent in mouse
230 skin but crucial in human nociception, and *TRPM8*-positive neuron organization differs between
231 rodents and primates (27). Given this translational gap to human physiology, we conducted a
232 similar comparative analysis using recent transcriptomic datasets composed exclusively of
233 human DRG cells (25, 27, 29), offering a more focused evaluation of the alignment of our pig
234 cell types with those in humans (Fig. S12). Here, we also observed a strong correspondence
235 between the cell types defined in our pig DRG taxonomy and those identified in human-specific
236 atlases.

237 These analyses further reinforce the notion that the pig serves as a robust model for studying
238 human sensory neurobiology, with pig DRG cell types closely aligning with those found in
239 humans, both within the broader cross-species context and within the more specific framework
240 of human-focused taxonomies.

241 Identification of C-OSMR-SSTs as probable sleeping nociceptors

242 Having described the pig DRG neuronal taxonomy and confirmed its validity to human DRGs,
243 we aimed to identify the subgroup which represents the sleeping nociceptors within those DRG
244 neuronal subtypes. CMi-fibers can be reliably identified in humans and pigs *in vivo* by a
245 combination of three functional electrophysiological characteristics. To transfer this *in vivo*
246 stimulation paradigm to our *in vitro* experiments, we applied our optimized Patch-seq
247 electrophysiological characterization pipeline (Fig. 3).

248 *First*, we applied a train of 75 suprathreshold stimulations delivered at 2 Hz to the patched cells
249 to assess activity-dependent slowing (ADS) (n=176 cells) (42). High amount of activity, e.g. due
250 to a 2 Hz stimulation in sleeping nociceptors in human or pig skin *in vivo*, induces substantial
251 slowing of conduction velocity (Fig. 3A,B,C, (22)). C-OSMR-SST neurons displayed more ADS
252 compared to other C-fiber related classes (Fig. 3D, Fig. S13). During the stimulation, the C-
253 OSMR-SST neurons displayed significant activity-dependent membrane potential
254 hyperpolarization, reduced AP peak and AP maximum upstroke slope relative to other C-fiber
255 cells (Fig. S13A-C).

256 *Second*, trains of twenty sine wave and square pulses were delivered at 4 Hz (i.e., sinus score, see
257 methods, n=213 cells) to assess the preference for sine waves versus square pulses observed *in*
258 *vivo* for sleeping nociceptors (13, 16, 22). The C-OSMR-SST subgroup demonstrated the highest
259 sinus score (Fig. 3E, right).

260 *Third*, trains of 20 short suprathreshold square pulses were delivered at 50 Hz (n=226 cells, Fig.
261 3F), as CMi fibers *in vivo* are unable to respond to high frequency stimulation continuously with
262 AP generation (i.e., they have a lower following frequency, (13, 16, 22)). The C-OSMR-SST
263 subtype displayed the fewest AP responses, significantly lower than the C-TAC1-KCNQ5, C-
264 TAC1-LRP1B, and C-LTMR subtypes (Fig. 3F, right).

265 To further validate our inference that C-OSMR-SST neurons likely correspond to sleeping
266 nociceptors (CMis), we conducted an independent analysis to determine whether neurons with
267 CMi-like electrophysiological features also express genes overlapping with C-OSMR-SST
268 markers. First, we performed a principal component analysis (PCA) on all included neurons

269 regardless of transcriptomic identity incorporating the three functional hallmarks of CMis—
270 ADS, sine wave affinity, and reduced following frequency at 50 Hz—along with AP duration
271 (Fig. 4A). As expected, the first principal component (CMi ephys PC1) accounted for the
272 majority of variance in these features (49%), indicating that this component could serve as a
273 single score for CMi-like neuronal identity. Leveraging gene expression profiles collected from
274 the same neurons via Patch-seq, we performed a transcriptome-wide analysis to identify genes
275 significantly associated with CMi scores (Fig. 4B). We found a substantial overlap between these
276 electrophysiology-based CMi-associated genes and markers of C-OSMR-SST neurons (Fig. 4C,
277 76 genes out of 228 total CMi-associated genes, p-value for hypergeometric test = 2.34×10^{-79}).
278 This analysis further highlighted several key pain-related ion channels, including *SCN11A* (Fig.
279 4D) and *SCN10A*, suggesting that their expression is closely related to CMi-like neuronal
280 characteristics and underscoring the potential future therapeutic value of targeting these channels
281 (see Discussion).

282 To establish a mechanistic linkage between the gene expression pattern and the functional
283 phenotype of C-OSMR-SST neurons we used the expression data of these neurons from the
284 snRNAseq dataset to generate a computational model based on an extension of the Hodgkin-
285 Huxley approach by using the modeling framework from (43) (see methods). In this model, for
286 instance, reduction of the SCN11A conductance of 50% leads to a strong reduction of the action
287 potential duration from 1.34ms to 1.18 ms (Fig. 4E, Fig. S14). The long action potential duration
288 as well as the action potential slope of C-OSMR-SST neurons was highly dependent on the
289 expression of SCN11A, suggesting this channel is a key player in shaping the characteristic
290 functional phenotype of CMi fibers.

291 Altogether, our *in vitro* experiments, modeled on adapted *in vivo* microneurography stimulation
292 protocols, demonstrate that C-OSMR-SST neurons exhibit functional properties similar to those
293 of CMi-fibers identified in human skin *in vivo*.
294

295 OSM selectively modifies CMi-fibers *in vivo* in humans

296 Our experiments suggest that C-OSMR-SST neurons are strong candidates for molecularly
297 defined CMi-fibers in pigs and humans. To show that OSMR is a functional marker selective for
298 human dermal sleeping nociceptors, we applied oncostatin-M (OSM), the activator of OSMR,
299 locally to the skin of healthy volunteers (Fig. 5A). As expected for CMi-activation in human skin
300 *in vivo* (44), we observed a widespread axon reflex erythema (i.e., skin redness) 24 h following
301 subcutaneous injection of OSM in four out of four participants (Fig. 5B, $275 \pm 108.3 \text{ mm}^2$).
302 Three participants did not report altered sensation, while one out of four participants experienced
303 moderate itch over several minutes post OSM injection (3 out of 10 on the numeric rating scale).
304 There was no itch or ongoing pain sensation for the next 24 h, apart from mechanical
305 hypersensitivity upon pressure.

306 We recorded two CMi- and two mechano-sensitive C-fibers (CM-fiber, polymodal nociceptors,
307 type 1a) with microneurography of the superficial fibular nerve in two healthy human volunteers
308 (schematic in Fig. 5C). ADS of two out of two recorded CMi-fibers was strongly reduced, if not
309 abolished, upon intracutaneous injection of OSM in the C-fiber's receptive field (Fig. 5D). In two
310 out of two mechano-sensitive CM-fibers, on the other hand, OSM injection did not result in any
311 observable ADS change (Fig. 5D).

313 In one participant, a recorded CMi-fiber shared its receptive field with a CM-fiber. Acutely
314 injecting OSM resulted in an immediate mechanosensory response in the CM- but not the CMi-
315 fiber (Fig. 5E). Seconds after OSM injection, we observed that the latency of the regularly
316 electrically induced APs of the CMi-fiber became unstable and latencies increased, indicating
317 fiber activity (Fig. 5E). Such changes, beyond the initial mechanosensory response, were not
318 observed in the CM-fiber. Based on the response of CMi-fibers – but not CM-fibers – to OSM,
319 we conclude that OSM application results in a selective reduction of ADS in human CMi-fibers
320 but not CM-fibers.

321 Thus, we provide evidence that CMi-fibers but not CM-fibers in the skin are affected by OSMR
322 application *in vivo*, making OSM-receptor expression by CMi but not CM likely. This suggests
323 that these CMi-fibers are likely to correspond to the molecular subgroup of C-OSMR-SST
324 neurons, identified by our multimodal taxonomy.

325 **DISCUSSION**

326 The research described here presents a major advance in our understanding of the molecular
327 underpinnings of sensory neurobiology and pain. We have defined a population of neurons
328 consistent with the elusive population of human dermal sleeping nociceptors, i.e., mechano-
329 insensitive C-fibers (CMis, type 1b), by bridging *in vivo* and *in vitro* physiology with multiple
330 single-cell transcriptomic techniques in pigs and humans. The unique strength and unprecedented
331 translational power of our data set lies in the direct link between functional and transcriptomic
332 data for each identified sensory neuron subtype. This allows us to paint the complex picture of
333 the molecular and functional identity of the CMis in human skin, laying the basis for drug target
334 identification, which may counteract their spontaneous activity observed during neuropathic pain
335 but keeps the warning function for potentially tissue damaging stimuli via other nociceptive
336 neurons functional (1–4).

337

338 C-OSMR-SST, the subgroup identified as CMis, express the highest level of *SCN1IA*, coding for
339 the voltage-gated sodium channel Nav1.9, which has been discussed intensely as drug target for
340 neuropathic pain (45, 46). We hypothesize that this channel, in combination with other channels
341 expressed in this neuron type, including *SCN10A*/Nav1.8, gives rise to the distinct functional
342 characteristics of C-OSMR-SST neurons, including sine wave sensitivity and formation of very
343 broad APs (45, 47). We included the sodium channel expression identified in this manuscript
344 into a basic computer model of CMi-fibers, based on (43). We identify the surprising
345 contribution of Nav1.9 to the steepness of the AP upstroke and the shoulder. Our findings thus
346 underscore the prominent role of Nav1.9 in CMi fiber electogenesis and the promise for
347 developing modulators of Nav1.9 channel function, as these might be especially effective in
348 silencing sleeping nociceptors. It is highly likely that more targets will emerge from our data set,
349 and future studies may show their translational and therapeutic potential.

350

351 OSM reduces activity dependent slowing and thus enhances excitability of CMis. Given the
352 involvement of OSM in the JAK pathway (48) and the high JAK1 Expression in the C-OSM-
353 SST subgroup, we speculate that the pathway we identified as molecular marker, involving JAK,
354 could be a potentially sensitizing pathway, which may change the CMi-fiber to a more CM-fiber
355 like phenotype during pathophysiological processes. A subset of CMi-fibers, which are
356 histamine sensitive, are associated with itch, and JAK-inhibitors are in clinical use as antipruritic
357 agents (49). The specific mechanisms of the contribution of CMi-fibers to itch and neuropathic
358 pain still remains to be elucidated. Interfering with JAK signaling may prevent CMi-fiber
359 sensitization and thus may potentially counteract the development of neuropathic pain and
360 chronic itch beyond its known anti-inflammatory effects (50, 51).

361

362 Our human experiments using microneurography demonstrate that CMis are responsive to
363 application of OSM, thus substantiating our transcriptomic inference that these cells express
364 OSMR. However, further disentangling how the application of OSM changes CMis, and
365 critically, whether OSM sensitizes CMis in the response to stimuli such as mechanical
366 stimulation, inflammatory agents, cold, heat, remains to be investigated and is beyond the scope
367 of the current study. We recognize that OSM-induced skin erythema in human volunteers
368 stretched out far beyond the actual injection site with blurred borders. Inflammation e.g. after
369 UVB irradiation causes a direct vasodilation independent from neuronal influence, the erythema

370 is – different to our observations - restricted to the site of injury and has sharp borders (52),
371 leading to our inference that OSM is directly acting on CMIs.
372

373 Our analyses demonstrate that the C-OSMR-SST cell type is highly transcriptionally conserved
374 across mammalian species. However, some genes, such as the nicotinic acetylcholine receptor
375 *CHRNA3*, were previously identified as a marker of sleeping nociceptors in mice (17, 53), but we
376 did not detect it in either of the three pig datasets presented in this study. In mice this neuronal
377 subgroup is mechano-insensitive in dissociated cultures but expresses nociceptor-related gene
378 products (17). These cells have few, if any, cutaneous afferents in mice. In line with this finding,
379 cutaneous sleeping nociceptors have been challenging to detect thus far in murine skin tissues in
380 contrast to humans and pig (54). Beside *CHRNA3*, recently, *TMEM100* has been described as a
381 marker involved in unsilencing of *CHRNA3*+ neurons in mice (53). As in human sensory
382 neurons (27), in our pig dataset *TMEM100* is expressed at very low levels in any neuron
383 type. We thus assume, that the transcriptomic identities of sleeping nociceptors differ between
384 skin and deep somatic tissues, or that CMi-fibers of mice and large, fur lacking mammals such as
385 human and pigs, differ significantly (17, 54).

386
387 A subset of CMi fibers can be activated by intense heating of the skin, typically at an average
388 surface temperature of $48.0 \pm 3.0^{\circ}\text{C}$ (9). However, this temperature threshold is painful for most
389 individuals, poses a risk of skin damage, and may not generate high enough temperatures in
390 deeper layers of the skin. Notably, intracutaneous injections of capsaicin in human skin activate
391 nearly all CMi fibers (13) suggesting that this fiber class could be triggered by heat stimuli if
392 they could be applied deeply enough in the skin.

393 As expected with our use of the 10X Genomics Single Cell 3' Kit, snRNAseq read coverage is
394 biased towards the 3' ends of gene bodies. Upon qualitative inspection, we observed that some
395 genes, including SCNA10A and TRPV1, exhibit unannotated reads in their 3' UTRs. We believe
396 this is likely due to incomplete annotation of the 3' UTRs in the reference transcriptome used.
397 However, this issue appears to be gene-specific, as other manually assessed genes, such as
398 CALCB, OSMR, and SST, do not show similar evidence of unannotated reads. Despite potential
399 suboptimal annotation for TRPV1 in pigs, we detected TRPV1 transcripts in a significant
400 number of C-OSMR-SST neurons, which aligns with human microneurography data showing
401 heat responsiveness in most CMi fibers.

402
403 In designating fiber types such as A β -, A δ -, and C-fibers in our study, we relied on gene
404 expression profiles and comparisons with existing transcriptomic datasets from large mammals
405 as well as on knowledge on fiber function in these species. While this allowed us to align our
406 classifications with well-characterized clusters, we acknowledge that distinguishing certain fiber
407 types, such as A δ - from C-fibers, remains challenging due to overlapping gene expression
408 patterns and species-specific differences (55).

409
410 The cell type identified with the highest transcriptomic similarities to the C-OSMR-SST cells are
411 the C-OSMR-GFRA1/2 neurons. The latter, however, show a very negative sine score and no
412 detected ADS arguing against CMi-fiber identity. In our Patch-seq data, we only identified two
413 cells of the C-OSMR-GFRA1/2 population. We note, however, that expression data of this

414 subgroup demonstrates a high *PIEZ02* level in pigs and humans, suggesting mechanosensitivity
415 (*56*). *PIEZ02* by itself is not solely responsible for mechanosensitivity in sensory neurons (*57*,
416 *58*), but it still indicates that the expressing cells are likely mechano-sensitive CM-fibers.
417

418 In conclusion, our work demonstrates the potential of our multi-modal peripheral sensory neuron
419 taxonomy as a powerful tool for identifying molecular markers of cell types that are highly
420 relevant to human pathophysiology, as we showed in the successful molecular identification of
421 human dermal sleeping nociceptors.

422
423

424 **MATERIALS AND METHODS**

425 **Blinding, Power analysis**

426 Besides psychophysical experiments, the study did not contain multiple study groups. Hence, the
427 investigators were not blinded during experiments and outcome assessment. There was no
428 predetermination of sample size with statistical methods. In psychophysical experiments the
429 volunteers were blinded for injection of OSM or control solution.

430 **Animals**

431 Patch-seq dataset and Visium spatial transcriptomics dataset

432 Dorsal root ganglia (DRG) of pigs were sampled according to the 3R criteria for reductions in
433 animal use, as leftovers from previous independent animal studies (e.g. LANUV reference no.
434 81-02.04.2018.A051). For this purpose, 10 female pigs of the German Landrace breed, with an
435 average age of 4.5 month and weight of 47.4 kg (SD 5.2 kg) were euthanized either using an
436 overdose of pentobarbital 60 mg/kg body weight or combination of exsanguination in deep
437 anaesthesia and overdose. Subsequently, the DRG were collected as described previously (59).
438 DRGs from all segments (cervical/thoracic/lumbar) were included in dataset generation.
439

440 **snRNAseq dataset**

441 Male domestic pigs (German Landrace) were euthanized according to ethical approval obtained
442 from the local authorities (RP Karlsruhe, Germany) under the approval number G-78/18.
443 Subsequently, thoracic and lumbar DRGs were quickly dissected, washed once in PBS and
444 stored overnight in RNAlater® at 4°C.

Biological replicate number	Protocol	Modification
1	(26)	None
2	(57)	+ FACS
3	(57)	+ FACS
4	(58)	None
5	(58)	None

445

446

447 **DRG tissue processing**

448 **Patch-seq DRG preparation**

449 DRG preparation was performed as in (59). Briefly, DRG of pigs were transferred on ice and
450 fine excision was performed in ice-cold DMEM F12 medium containing 10% FBS. DRG were
451 treated with 1 mg/ml collagenase P, 1 mg/ml trypsin T1426 and 0,1 mg/ml DNase for digestion.

452 DRG were cut into small pieces inside the digestion medium for surface enlargement. DRG were
453 incubated in 37°C, 5% CO₂ for 120 minutes ± 30 minutes. Approximately after 60 minutes in
454 digestion medium, DRG were triturated using a plastic pipette. After the full incubation time,
455 DRG were triturated three times using glass pipettes with decreasing tip diameter. For further
456 purification, DRG were centrifuged at 500 x G and 4°C twice for four minutes each and the
457 pellets were suspended in DMEM F12 with 10% FBS. DRG were subsequently separated from
458 the lighter cell fragments and myelin by centrifugation of a Percoll gradient containing a 60%
459 Percoll and a 25% Percoll gradient for 20 minutes at 500 x G. DRG neurons were plated on
460 coverslips coated with poly-D-lysine (100 µg/ml), laminin (10 µg/ml) and fibronectin (10 µg/ml).
461 Neurons were then cultured in Neurobasal A medium supplemented with B27, penicillin,
462 streptomycin and L-glutamine and used for voltage-clamp recordings after 12-72 hours in
463 culture.

464 Addition of recombinant NGF, frequently used in DRG cultures, has been described to decrease
465 the fraction of mechanical insensitive fibers and decrease the amount of ADS in mechanical
466 insensitive fibers (17, 60). Therefore, we avoided the use of NGF in all our experiments.
467

468 snRNAseq DRG preparation

469 12-16 hours after euthanasia, adjacent fat tissue and the nerve root and spinal nerve were
470 trimmed from the DRGs under a dissecting microscope. The cleaned DRGs were flash-frozen in
471 liquid nitrogen and stored at -80°C until use for nuclei isolation.

472 Nuclei were isolated from 80 mg thoracic and lumbar DRG tissue per sample employing
473 previously published protocols (27, 61, 62) that differ with respect to tissue lysis conditions
474 (Triton X-100 or IGEPAL CA-630) and strategies employed for separation of debris and nuclei
475 (40 µm filtration plus iodixanol density gradient centrifugation or 40 µm filtration plus
476 magnetic-assisted enrichment of neurons using rabbit polyclonal anti-NeuN antibody (Millipore,
477 cat# ABN78, dilution 1:5,000) and anti-rabbit IgG microbeads (Miltenyi Biotech, cat# 130-048-
478 602, dilution 1:5)). The protocol by Ernst et al. that only relies on 40 µm filtration was modified
479 to include an additional step of fluorescence-assisted enrichment of neuronal nuclei after the
480 final two nuclei washing steps of the protocol (61). For this purpose, the nuclei were stained with
481 Anti-NeuN-Alexa Fluor 555 (Millipore, cat# MAB377A5, dilution 1:100) for 30 minutes at 4°C
482 on a rotator and subsequently with DAPI for 5 minutes on ice. At the FlowCore Mannheim,
483 double-positive singlets were sorted into PBS/1% BSA using a BD FACSAria IIu equipped with
484 a 100 µm nozzle. All protocols resulted in similar high-quality nuclei (based on microscopic
485 inspection) and were therefore used as input for microfluidics-based generation of single-nucleus
486 gene expression libraries.
487

488 Visium spatial transcriptomics DRG preparation

489 Lumbar DRGs from female domestic pigs (German Landrace) were recovered shortly after
490 euthanasia. The tissue was trimmed of any fat or connective tissue, rinsed once with artificial
491 cerebrospinal fluid, and then freshly frozen by burying it in pulverized dry ice for 1 minute at the
492 time of extraction. All DRGs were subsequently stored in a -80°C freezer. 22 fresh-frozen DRGs
493 from the lumbar region of 7 female pigs were embedded in optimal cutting temperature (OCT)
494 using a cryomold placed over dry ice. To avoid thawing, the OCT was poured in small volumes
495 surrounding the tissue. Two sections of the embedded tissue were cryosectioned at 10 µm, 200
496 µm apart from each other to ensure different neurons were sliced. The sections were mounted

497 onto SuperFrost Plus charged slides for staining with Eosin and Hematoxylin (HE) or on the
498 capture area of Visium slides for spatial sequencing, while avoiding folding or overlapping.

499 Patch-seq Recording Procedures

500 Patch-Solutions

501 Extracellular solution contained (in mM): 140 NaCl, 3 KCl, 1 MgCl₂, 1 CaCl₂, 10 HEPES, 20
502 glucose (pH 7.4; 300-310 mOsm). Intracellular solution contained (in mM): 4 NaCl, 135 K-
503 gluconate, 3 MgCl₂, 5 EGTA, 5 HEPES, 2 Na₂-ATP, 0.3 Na-GTP (pH 7.25; 290-300 mOsm).
504 To minimize RNase contamination of the intracellular solution (ICS), 100x stock solutions of
505 each component (except ATP and GTP) were made using RNase-free H₂O or DEPC-treated and
506 autoclaved where appropriate. Afterwards, the final ICS was manufactured by adding GTP, ATP
507 and RNase free water. Osmolality control was performed.
508

509 Patch-Clamp Recordings

510 Experiments were performed using a HEKA EPC 10USB amplifier and PatchMaster and
511 analyzed using FitMaster v2.8 software (all HEKA electronics, Lambrecht, Germany). Pipette
512 resistance was 1.5-3.5 MΩ. Currents were low-pass filtered at 10 kHz and sampled at 100
513 kHz. The liquid-junction-potential was corrected for +14.3 mV. All experiments were performed
514 at room temperature. After reaching giga-seal and pipette capacitance correction, the whole cell
515 configuration was established. The resting membrane potential (RMP) was measured
516 immediately after establishing the whole-cell configuration. Holding current was then adjusted to
517 achieve a membrane voltage of -60 ± 3 mV.

518 The sequence of applied pulse protocols was as follows: First, APs were elicited with 200 ms
519 square pulse depolarisations of increasing intensity. Then, 4 Hz rectangular and 4 Hz sinusoidal
520 depolarization pulses were injected with a 5 second break in between to confirm the threshold
521 and compare also longer rectangular threshold with the sinusoidal threshold (sinus_score). This
522 was followed by 20 4 ms rectangular injections of 1000 pA at 2, 5, 10, 25, 50 and 100 Hz for
523 assessment of the maximum follow frequency. Afterwards, the threshold for 500 ms halfsinus-
524 shaped injections was assessed. Finally, a protocol of 75 1000 pA 10 ms rectangular pulses were
525 injected for assessment of changes in slope, membrane potential, AP peak and rising time
526 changes upon repetitive stimulation as a measurement of axonal slowing (42). The
527 electrophysiological assessment of one cell takes around 11 minutes.
528

529 mRNA harvesting for Patch-seq

530 Given the large size of pig DRG neurons, the sample collection followed a procedure using two
531 separate pipettes as follows (Fig. S1): First, the recording pipette was retracted under slightly
532 negative pressure from the cell and immutably broken into in PCR-tube containing 4 µl of lysis
533 buffer (40 mM Guanidine hydrochloride, 0.1 mM Smart dT30VN primer, 5 mM dNTPs),
534 secondly a second larger pipette with diameter customized for cell diameter of the cell to collect
535 (resistance ~0.7 MΩ) was used to collect the entire cell. After collection, this pipette was
536 broken into the same PCR-tube. Samples were immediately frozen on dry ice. Complete and
537 exclusive collection was documented with the microscope's camera.
538

539 Extraction of electrophysiological features

540 Electrophysiological feature extraction was performed using in-house scripted IGOR procedures.
541 The first AP evoked by the square pulse protocol was used to calculate the AP properties. The
542 AP threshold was defined as the minimum of the first derivative of the AP (= the point of

inflection during the depolarization). The afterhyperpolarization is the minimum after the AP peak. The amplitude is measured between RMP and AP peak. To calculate the AP half-width, the half distance between threshold and peak is measured and the distance between this point during depolarization and repolarization is evaluated. The time to peak is the duration between current pulse onset and AP peak. The maximum slope of the upstroke was calculated between threshold and peak, whereas the slope of the subthreshold depolarization was determined between RMP and threshold. Overshoot slope was calculated for the part exceeding 0 mV. Sine wave affinity (sine_score) was calculated as the difference in the number of spikes between 20 sinusoidal and 20 rectangular stimulations (theoretical maximum = 20 (20 sine spikes vs 0 rectangular spikes), theoretical minimum = -20 (0 sine spikes vs 20 rectangular spikes)). Following frequency (FF) is given as the number of spikes elicited by 20 stimulations for each stimulation frequency.

Half Sine Threshold was defined as amount of current injection in which the AP was elicited during half sine stimulation.

Activity dependent Time to Peak delay was extracted as the change in time to peak in milliseconds compared to the first AP evoked by 75 suprathreshold stimulations. Activity dependent change in resting membrane potential is given as change in mV of the membrane potential during stimulation compared to potential before stimulation by 75 suprathreshold square voltage pulses. Activity dependent change in slope is given as maximum in first deviation of AP train normalized to value of first AP evoked by 75 stimulations.

563 RNA-Sequencing

564 snRNAseq dataset

565 Construction of single-nucleus gene expression libraries and sequencing

At the next generation sequencing core facility of the Medical Faculty Mannheim at Heidelberg University, single-nucleus solutions were subjected to barcoding, reverse transcription and gene expression library construction using the 10XGenomics microfluidics platform (Chromium controller and Next GEM Single Cell 3' v3.1 (sample 1-3) or of Multiome Kit (sample 4-5)) according to the manufacturer's instructions. Gene expression libraries were sequenced on an Illumina NextSeq550.

572 snRNAseq data analysis

Sequencer output files were converted into fastq-files using Cellranger 6.0.1 mkfastq. Using Cellranger 6.0.1 count, reads were then mapped to the pig genome (Sscrofa11.1 with Ensembl 105 annotation) on the bwForcluster Helix high-performance computing system. Reads uniquely mapping in sense to the transcriptome (exon and intron) were then used to quantify transcript abundances using unique molecular identifiers (UMI). After cell calling, which is also built into Cellranger 6.0.1, a cell-gene expression matrix was generated and imported into R (version 4.2.2, RStudio version 2022.12.0) for further analysis using Seurat (version 4.3.0.9001). Nuclei with less than 200 detected UMIs and doublets (identified with DoubletFinder) were filtered out. For each replicate, mitochondrial reads were regressed out during count normalization with "SCTransform" v2. Normalized data was then used for anchor-based data integration resulting in an integrated data assay. This data assay (variable features set to 3,000) was used for dimensional reduction by principal component analysis. The first 30 principal components were used to visualize nuclei in two dimensions using uniform manifold approximation and projection (UMAP). Similarly, the first 30 principal components were used for cluster analysis setting the resolution parameter of "FindClusters" to 2. Clusters with high percentage of mitochondrial genes or low number of DEGs likely reflect empty droplets and were therefore removed from the

589 dataset. The resulting dataset (16,979 neuronal and non-neuronal nuclei) was subset to neurons
590 based on the expression of SNAP25, SCN9A, THY1, TAC1, and RBFOX1 (pan-neuronal
591 markers of human DRG neurons (27)). A neuronal set of 3,000 variable features was identified
592 and dimensional reduction, two-dimensional projection and cluster analysis was repeated with
593 the same parameters. This resulted in 18 clusters, three of which were merged based on similar
594 marker gene expression. Finally, annotation of the 16 final clusters was performed based on the
595 presence/absence of marker genes used to distinguish transcriptionally-defined sensory neurons
596 in mice (30, 39, 63–66), monkey (25, 26) and human (25, 27, 29).
597

598 Patch-seq Dataset

599 Sequencing

600 Sequencing and pre-processing

601 Individual lysed cells were treated according to the Smart-Seq2 library preparation protocol (67).
602 Preamplified cDNA was quantified and the average size distribution was determined via D5000
603 assay on a TapeStation 4200 system (Agilent). Tagmentation and subsequent next-generation
604 sequencing (NGS) library generation were performed using 200 pg of cDNA. NGS libraries were
605 quantified by High-Sensitivity dsDNA assay on a Qubit (Invitrogen) and the average size
606 distribution was determined via D5000 assay on a TapeStation 4200 system (Agilent). Libraries
607 were equimolarly pooled, and sequenced SR 75bp on a NextSeq500 system with a 75 cycles
608 High Output v2 chemistry or NextSeq2000 with a P2 or P3 100 cycles flow cell (Illumina). Raw
609 sequencing data were demultiplexed and converted into fastq format using bcl2fastq2 v2.20.
610 After quality checking with MultiQC v.1.5, reads were pseudoaligned to the Sus Scrofa genome
611 11.1 (104, Ensembl) via Kallisto v.0.440 with default parameters. Patch-seq cell samples with
612 fewer than 10,000 reads were discarded.
613

614 Spatial Transcriptomics Dataset

615 Fixation, Staining and Imaging

616 Methanol fixation and Eosin and Haematoxylin staining for an initial tissue quality control
617 analysis was performed as described in the 10XGenomics Methanol Fixation, H&E Staining &
618 Imaging for Visium Spatial Protocols (Demonstrated Protocol CG000160). We stained a total of
619 60 sections, each 10 µm in thickness, from 22 fresh frozen DRG obtained from 7 female pigs.
620 These sections were mounted within the capture areas of 11 Visium slides that contained 55-µm
621 printed barcoded spots. Imaging was conducted using the manual load and the fluorescence
622 features of an Olympus vs120 Slide Scanner.
623

624 Tissue Optimization

625 Different permeabilization times (3, 6, 12, 18, 24 and 30 minutes) were evaluated following the
626 10XGenomics Visium Spatial Gene Expression Reagent Kits - Tissue Optimization User Guide
627 CG000238 Rev E. This protocol required the reagents from the Visium Spatial Tissue
628 Optimization Reagent Kit, PN-1000192 (stored at -20°C) and the Visium Spatial Tissue
629 Optimization Slide Kit PN-1000191 (stored at ambient temperature). The exposure time of the
630 permeabilization enzyme was 18 minutes based on the analysis of the tissue optimization
experiment
631

632 10XGenomics Visium Spatial protocols

633 We used the spatial sequencing protocol Visium Spatial Gene Expression Reagent Kits, 16 rxns
PN-1000186 and Library Construction Kits, 16 rxns PN-1000190. All reagents were stored at -

634 20°C. Additionally, Visium Spatial Gene Expression Slide Kits, 16 rxns PN-1000185 were
635 acquired and stored at ambient temperature.
636 The protocol was performed exactly as stated in the Visium Spatial Gene Expression Reagents
637 Kits User Guide CG000239 Rev F. It consisted of a 5-step process, starting with
638 permeabilization and reverse transcription (step 1). The exposure time of the permeabilization
639 enzyme was 12 minutes based on the analysis of the tissue optimization experiment. After
640 second strand synthesis and denaturation (Step 2), the samples were prepared for a full-length
641 cDNA amplification via Polymerase Chain Reaction (PCR) (step 3). Afterwards, a Visium
642 spatial gene expression library was generated (step 4), followed by sequencing (step 5). Steps 4
643 and 5 were performed at the Genomics Core facilities of the University of Texas at Dallas. The
644 samples were sequenced using the Illumina NextSeq2000 Sequencing system.

645 [Visium spatial RNA-seq analysis](#)

646 From our sequencing run, we obtained a total average of 59,081,551 M reads, 86.51% of the
647 reads were mapped with 84.22% confidence. We detected an average of 13,870 genes and 1574
648 barcodes under tissue. The mean of reads per barcode was 40,490, and the median of Unique
649 Molecule Identifier (UMI) counts per spot was 2,819. The generated Illumina BCL files were
650 processed with the 10XGenomics pipeline (Space Ranger v1.1). This pipeline allowed the
651 alignment of the FASTQ files with bright-field microscope images and the pig reference
652 transcriptome (Sscrofa11.1). Using the Loupe Browser (v4.2.0, 10x Genomics), we visualized
653 the location of the barcoded mRNAs for downstream analysis by selecting the barcoded spots
654 overlapping single neurons. We identified 6408 barcodes overlapping single neurons and 12,304
655 overlapping multiple barcodes. To avoid double counts, we excluded the barcodes overlapping
656 multiple neurons. As part of a quality control step, we removed neuronal barcodes with less than
657 a hundred reads and no counts of the neuronal marker Synaptosome Associated Protein 25
658 (SNAP25) using Python (v3.8 with Anaconda distribution).

659 [Visium spatial morphology measurements](#)

660 We compiled a .csv file containing the positional data (coordinates) of barcodes overlapping with
661 single neurons per Visium capture frame. Subsequently, we employed Cellsens imaging software
662 to visualize the corresponding .tif image files and identify the neurons. Within this software, we
663 utilized the polyline measuring tool to determine the diameter of neurons (μm) exhibiting distinct
664 DAPI nuclear staining, indicating their sectioning within the central region of the cell. Cells
665 displaying cytoplasmic distortion attributed to freezing artifacts were excluded from our
666 measurements.

667 [RNA-seq dataset integration](#)

668 [Pig cross-dataset genomics dataset integration and cell type mapping](#)

669 We used the pig snRNAseq dataset as a reference to integrate each of our additional pig datasets
670 separately, ensuring precise cell-type mapping across species and technologies. The datasets
671 integrated with this reference include Patch-seq data from pigs, and a separate 10X Visium
672 spatial transcriptomics dataset from pigs. In our integration process, the Patch-seq dataset
673 featured 22,259 genes and the pig 10X Visium had 15,924 genes. To align these with our pig
674 snRNAseq reference, which contains 30,477 genes, we used the intersection of the gene symbols
675 across each pair of datasets. To integrate Patch-seq transcriptomes with the snRNAseq reference
676 dataset, we used the Canonical Correlation Analysis (CCA) workflow from Seurat (v4.3.0). We
677 performed dataset integration by treating the Patch-seq data as coming from a single separate
678 batch, re-integrated all samples across all batches, using SCTtransform v2 normalization with

679 mitochondrial reads regressed out. We selected 6,000 highly variable genes as anchor integration
680 features to integrate data across batches into a single integrated atlas object using the
681 SelectIntegrationFeatures function. The datasets were then integrated using the IntegrateData
682 function with the ‘normalization.method’ parameter set to “SCT”, and ‘k.weight’ set to 75. Next,
683 we performed principal component analysis (50 dimensions), and UMAP on the first 30 principal
684 components for dimensionality reduction and visualization purposes.

685 To assign cell-type labels to the Patch-seq sampled cellular transcriptomes, we used a K-nearest
686 neighbour approach based on the 20 nearest reference snRNAseq neighbours using the first 30
687 PCA dimensions. The nearest neighbours for each Patch-seq cell were first defined using
688 FindNeighbors in Seurat, then identified using the function TopNeighbors with k parameter of
689 20. Each Patch-seq neuron’s cell type was defined as the most frequent snRNAseq-based cell
690 type present in the nearest 20 neighbours.

691 We used a modified approach of the above for integrating the pig 10X Visium dataset and to
692 map assigned cell-type labels, due to the larger size of the 10X Visium datasets relative to the
693 snRNAseq data. For the 10X Visium dataset, we iterated through batches of a maximum size of
694 250 cells within each donor to facilitate using the same parameters for the integration and cell
695 type mapping procedure as were used for integration and cell-type mapping of the Patch-seq
696 data.

697 Analysis of species and dataset-specific transcription profiles

698 To identify transcriptional markers of each DRG neuron subtype, we used the FindAllMarkers()
699 function from Seurat (v4.3.0) separately on each collected dataset. We set the parameters min.pct
700 and logfc.threshold to -Inf, min.cells.feature and min.cells.group to 1 to maximize the number of
701 genes tested for comparison across the datasets.

702 Transcriptome marker gene correlation analyses

703 To determine agreement of transcriptional markers across the datasets, for each dataset, we used
704 the output of the FindAllMarkers() function from Seurat to compute enrichment fold changes
705 (avg_log2FC) of each gene from each cell-type in comparison to all other cells in the dataset.
706 Next, we intersected the lists of enriched genes from each cell type between pairs of datasets and
707 correlated enrichment values across intersecting genes. We then used the cor.test() function in R
708 with the method parameter set to "spearman" to correlate the avg_log2FC values for each gene
709 across the two datasets.

710 Principal Component Analysis (PCA) of Electrophysiological Features:

711 Electrophysiological data from patch-clamp recordings were extracted for four key features
712 associated with CMi-like properties: action potential duration (APD), response to 50 Hz
713 stimulation (50Hz), sinus score, and relative activity-dependent slowing (Rel. ADS). To address
714 missing values in the dataset, we employed k-nearest neighbor (kNN) imputation using the
715 recipes package in R. The imputation step used 5 neighbors ($k = 5$) to estimate missing values
716 based on similar cells in the multidimensional feature space. This approach preserves the overall
717 structure of the data while allowing for complete case analysis in subsequent steps.

718 Following imputation, the four electrophysiological features were scaled and centered. We then
719 performed Principal Component Analysis (PCA) using the prcomp function in R. The first two
720 principal components were used for further analysis and visualization. We created a biplot to
721 display both the distribution of cells in the PC space and the contributions of each
722 electrophysiological feature to the principal components. Cell types were color-coded, and
723 feature loadings were displayed as vectors on this plot.

724 CMi associated differential expression analysis:
725 To identify genes associated with CMi-like properties, we performed differential expression
726 analysis using the limma-voom pipeline. The CMi score (PC1 from the electrophysiological
727 PCA) was used as a continuous variable in the design matrix. Genes with an adjusted p-value <
728 0.05 and ABS(log2 fold change) > 0.5 were considered significantly differentially expressed.
729

730 Cross-species cell type replicability and prediction
731 We compared our pig snRNA-seq dataset to the cross-species DRG atlas from Bhuiyan et al.
732 (2024) using two complementary approaches: MetaNeighbor for cell type replicability
733 assessment and Seurat's label transfer for cell type prediction.
734

735 Metaneighbor analysis
736 MetaNeighbor (version 1.16.0) was used to assess cell-type replicability between our pig
737 snRNA-seq data and the cross-species atlas. MetaNeighbor constructs a network of rank
738 correlations among all cells based on shared variable genes, using the principle that cells
739 belonging to the same subtype exhibit more correlated gene expression patterns than distinct cell
740 types. By applying a neighbour voting system, each cell accrues a score denoting the proportion
741 of its neighbours sharing its cell type. This metric is quantified by the area under the receiver
742 operator characteristic curve (AUROC), with the mean AUROC across folds determining the
743 degree of cell type similarity. The unsupervised procedure requires a gene-by-cell matrix in
744 SummarizedExperiment format, along with metadata identifying dataset and cell-type labels for
745 each cell. We followed the unsupervised MetaNeighbor procedure described in detail with
746 accompanying scripts labelled Procedure 1 at <https://github.com/gillislab/MetaNeighbor-Protocol/> (68). We identified 1172 highly variable genes using the variableGenes() function.
747 These genes were input for MetaNeighborUS() to generate a cell-cell similarity network and
748 quantify cell type replicability. The output is a cell type by cell type mean AUROC matrix, with
749 higher values indicating greater similarity. We used MetaNeighborUS() with parameters
750 one_vs_best = TRUE and symmetric_output = FALSE to identify the best matches between pig
751 and atlas cell types. A cluster graph was created using makeClusterGraph() (low_threshold =
752 0.3) and visualized with plotClusterGraph() to represent cell type relationships across the
753 datasets.
754

755 Label transfer analysis
756 To predict cell types for our pig snRNA-seq data, we used Seurat's label transfer workflow
757 (version 4.3.0.1), employing the same cross-species DRG atlas as a reference using its
758 'Atlas_annotation' cell-type labels. The pig snRNA-seq data was preprocessed using standard
759 Seurat functions (NormalizeData, FindVariableFeatures, ScaleData, RunPCA). We used
760 FindTransferAnchors() to identify anchors between the atlas and the pig data, specifying "RNA"
761 as the assay and "cca" as the reduction method. TransferData() was then applied to transfer cell
762 type labels from the atlas to the pig dataset. Finally, we used MapQuery() to project the pig data
763 onto the UMAP space of the atlas for visualization and comparison of predicted cell types.
764

765 Computational action potential modeling
766

768 We used computational modeling to study the impact of SCN11A abundance on the AP
769 morphology. We adapted the modeling framework from (43) to C-OSMR-SST neurons. The
770 model considers SCN1A-5A & 8A-11A and is based on an extension of the Hodgkin-Huxley
771 approach which accounts for non-exponential inactivation kinetics and shows better agreement
772 to data. The gating parameters were fitted based on voltage clamping data and are taken from
773 (43). The contribution of a given sodium channel subtype to the total sodium conductance is
774 chosen according to its expression level in C-OSMR-SST neurons. The APs were generated by a
775 current injection of $30\mu\text{A}/\text{cm}^2$ starting at time 0 and lasting until the end of the observation
776 period. The AP width was measured at the threshold voltage which was determined using the
777 second derivative of dV/dt with respect to V as described in (69).

778

779 In vivo experiments

780 Pig

781 All experimental interventions in pigs were approved by the regional ethics council in Karlsruhe,
782 Baden-Wuerttemberg, Germany (G-78/18). *In vivo* extracellular recordings from the “teased”
783 saphenous nerves were performed using DAPSYS software (www.dapsys.net) (70). Briefly,
784 electrical rectangular pulses (0.5 ms duration; 20 mA intensity; 0.25 Hz) were delivered by a
785 constant current stimulator (DS7A, Digitimer Ltd., Hertfordshire, UK) via two non-insulated
786 microneurography electrodes (FHC Inc., Bowdoin, ME, USA), inserted intradermally at sites
787 where time-locked action potentials with long latencies could be elicited (22). At the end of the
788 experiment, pigs were euthanized by i.v. injection of 10 ml Tanax (T-61, Intervet Deutschland
789 GmbH) and death was confirmed by induction of lasting electrical silence on ECG and
790 disappearance of carotid pulse.

791 Human

792 OSM experiments

793 Recombinant Human Oncostatin-M protein, carrier free (Biotechne, Minneapolis, Minnesota,
794 U.S., REF Number: 8475-OM-050/CF), diluted in 20 μl sterile synthetic interstitial fluid (SIF)
795 (71) was injected intracutaneously into human volunteers, who provided informed consent. The
796 experiments were conducted on independent researchers who are all senior co-authors of this
797 study (self-experiments). SIF contained (in mM) 107.8 NaCl, 3.5 KCl, 1.5 CaCl₂, 0.7 MgSO₄,
798 26.2 NaHCO₃, 1.7 NaH₂PO₄, 9.6 sodium gluconate, 5.5 glucose, and 7.7 sucrose with a stable
799 pH of 7.4. The test person was blinded towards the applied substances during experiments.

800 Superficial blood flow

801 Superficial blood flow was assessed by a laser Doppler imager (LDI, Moor Instruments Ltd.,
802 Devon, United Kingdom) or a laser speckle imager (FLIPI2, Moor Instruments Ltd., Devon,
803 United Kingdom with measurement software V2.0). Baseline images were taken before and 24 h
804 after the injections. Erythema areas were calculated as those pixels exceeding the mean flux
805 value + 2-fold standard deviation measured in a control area between the injection sites using
806 moorLDI Software (Research Version 5.3, 2009, Moor Instruments Ltd) and for laser speckle
807 data moorFLPI-2 software (Review Software V 5.0, Moor Instruments Ltd)).

808 Experimental protocol for psychophysics

809 10 μl in SIF diluted OSM and SIF alone as control were intracutaneously injected at the volar
810 forearms of healthy volunteers in a blinded approach. Thereafter ratings were assessed verbally
811 every 10 seconds for 5 minutes on a rating scale from 0 (no pain/itch) to 10 (maximally
812 imaginable itch/pain) and skin vasodilation was measured using either laser Doppler or laser

813 speckle imaging as described above. Thereafter, and 24 h after skin injection, vasodilation via
814 Laser speckle and laser Doppler imaging and hyperalgesia were assessed using manual pressure,
815 mechanical impact and von Frey filament stimulation.

816 [Microneurography](#)

817 Experiments were conducted at the University of Aachen, microneurography protocols were
818 approved by the local ethics committee (EK 143/21) and are registered within the German
819 Registry for Clinical Studies (DRKS00025261). APs of single C-fibers from cutaneous C-fiber
820 fascicles of the superficial peroneal nerve were recorded as previously described (10, 72).
821 A tungsten recording needle (Frederick-Haer, Bowdoinham, ME, USA) is inserted and placed
822 close to an unmyelinated afferent nerve fiber bundle. After reaching a stable position, C-unit
823 innervation territories are detected using a pointed electrode (0.5 mm diameter) delivering
824 electrical pulses.

825 C-fiber units are identified by their low conduction velocity (< 2 m/s). A pair of 0.2 mm diameter
826 needle electrodes (Frederick-Haer company) is inserted into the previously located innervation
827 territory for intracutaneous stimulation of the recorded C-fibres. Low repetition rates are inserted
828 using a Digitimer DS7 constant current stimulator. The signal is amplified, filtered and stored on
829 a computer using custom-written microneurography software DAPSYS and analyzed offline
830 using DAPSYS (Brian Turnquist, <http://dapsys.net>) and Microsoft Excel.

831 Single C-fibers were differentiated by their individual conduction latency during continuous low
832 frequency stimulation (0.25 Hz; intensity at least 1.5 times the individual electrical fiber's
833 threshold). After recording C-fiber responses, we used the "marking technique" to characterize
834 the units. This is based on the slowing of conduction velocity when a C-fiber conducts more than
835 one AP within a short time period, which is known as activity-dependent conduction velocity
836 slowing (ADS). The amount of ADS strongly correlates with the number of additional APs
837 conducted in the seconds before the electrically induced AP.

838 To determine the mechanical sensitivity of the recorded C-fibers, we repetitively applied
839 mechanical stimuli using stiff von Frey filaments of 22 g (Stoelting, Chicago, IL, USA) in the
840 receptive fields.

841 We assigned C-fibers as mechanosensitive (CM) or mechano-insensitive (CMi) according to
842 their mechanical responses and electrophysiological properties. C-fibers with an ADS < 5% of
843 their initial latency to an electrical stimulation protocol with rising frequencies (20 pulses at
844 0.125 Hz, 20 pulses at 0.25 Hz, 30 pulses at 0.5 Hz), a normalization of latency thereafter of
845 more than 43% within 20 s, and a response to < 22 g von Frey stimulation, were classified as
846 CM-fibers. C-fibers with an ADS > 5% and a recovery of < 43% and no mechanical response to
847 75 g von Frey stimulation were classified as CMi-fibers.

848 [Experimental protocol for microneurography](#)

849 First the C-fibers were classified into CM and CMi as described above. In 50 healthy participants
850 2 Hz stimulation was performed for 3 minutes. Part of those data were utilized for comparison to
851 patch clamp data (see figure 3). In the self-experiments in a different experimental setup during
852 continuous 0.25 Hz electrical stimulation of the fibers in the receptive field in the skin 20 µl of
853 OSM was injected intracutaneously directly under the stimulation needles. Thus, OSM affected
854 maximally 5 mm of the nerve fibers. Continuous electrical stimulation is necessary for using the
855 marking method for assessing fiber activation and changes in biophysical properties (72).

856 [Statistics](#)

857 All statistical analyses were conducted using R (version 4.2.1). Non-parametric tests, including
858 the Wilcoxon Rank-Sum Test and the Mann-Whitney U Test, were applied to evaluate median

859 differences in data sets that were not assumed to follow a normal distribution. The Kruskal-
860 Wallis Test was used for comparing medians across multiple groups, while the Welch's t-test
861 was used to compare means between two groups with unequal variances. For analyses involving
862 multiple group comparisons, ANOVA was used to ascertain mean differences, followed by
863 Tukey's Honest Significant Difference (HSD) Test for post-hoc pairwise comparisons to control
864 for multiple testing errors. Specifics regarding the number of observations, p-values, and the tests
865 used are reported in the figure legends or directly in the main text as appropriate.
866 Principal component analysis was performed with Graphpad PRISM (version 10.2.0) on
867 standardized data. Principal components were included that together explained >75% of the total
868 variance.

869

870

871

872 **List of Supplementary Materials**

873 Figs. S1 to S15

874 Table S1

875 Data S1 to S2

876

877

878 **References and Notes**

- 879 1. I. P. Kleggetveit, B. Namer, R. Schmidt, T. Helås, M. Rückel, K. Ørstavik, M. Schmelz, E. Jørum, High
880 spontaneous activity of C-nociceptors in painful polyneuropathy. *Pain* **153**, 2040–2047 (2012).
- 881 2. J. L. Ochoa, M. Campero, J. Serra, H. Bostock, Hyperexcitable polymodal and insensitive nociceptors in painful
882 human neuropathy. *Muscle Nerve* **32**, 459–472 (2005).
- 883 3. K. Sauerstein, J. Liebelt, B. Namer, R. Schmidt, R. Rukwied, M. Schmelz, Low-Frequency Stimulation of Silent
884 Nociceptors Induces Secondary Mechanical Hyperalgesia in Human Skin. *Neuroscience* **387**, 4–12 (2018).
- 885 4. R. Schmidt, M. Schmelz, H. E. Torebjörk, H. O. Handwerker, Mechano-insensitive nociceptors encode pain
886 evoked by tonic pressure to human skin. *Neuroscience* **98**, 793–800 (2000).
- 887 5. J. Serra, H. Bostock, R. Solà, J. Aleu, E. García, B. Cokic, X. Navarro, C. Quiles, Microneurographic
888 identification of spontaneous activity in C-nociceptors in neuropathic pain states in humans and rats. *Pain* **153**, 42–
889 55 (2012).
- 890 6. B. Namer, H. O. Handwerker, Translational nociceptor research as guide to human pain perceptions and
891 pathophysiology. *Exp Brain Res* **196**, 163–172 (2009).
- 892 7. J. Serra, M. Campero, J. Ochoa, H. Bostock, Activity-dependent slowing of conduction differentiates functional
893 subtypes of C fibres innervating human skin. *J Physiol* **515** (Pt 3), 799–811 (1999).
- 894 8. M. M. Düll, K. Riegel, J. Tappenbeck, V. Ries, M. Strupf, T. Fleming, S. K. Sauer, B. Namer, Methylglyoxal
895 causes pain and hyperalgesia in human through C-fiber activation. *PAIN* **160**, 2497 (2019).
- 896 9. M. Schmelz, R. Schmidt, C. Weidner, M. Hilliges, H. E. Torebjörk, H. O. Handwerker, Chemical response
897 pattern of different classes of C-nociceptors to pruritogens and algogens. *J Neurophysiol* **89**, 2441–2448 (2003).
- 898 10. M. Schmelz, R. Schmidt, A. Bickel, H. O. Handwerker, H. E. Torebjörk, Specific C-receptors for itch in human
899 skin. *J Neurosci* **17**, 8003–8008 (1997).
- 900 11. J. Serra, M. Campero, H. Bostock, J. Ochoa, Two types of C nociceptors in human skin and their behavior in
901 areas of capsaicin-induced secondary hyperalgesia. *J Neurophysiol* **91**, 2770–2781 (2004).
- 902 12. O. Obreja, R. Rukwied, L. Nagler, M. Schmidt, M. Schmelz, B. Namer, Nerve growth factor locally sensitizes
903 nociceptors in human skin. *Pain* **159**, 416–426 (2018).
- 904 13. R. Jonas, B. Namer, L. Stockinger, K. Chisholm, M. Schnakenberg, G. Landmann, M. Kucharczyk, C. Konrad,
905 R. Schmidt, R. Carr, S. McMahon, M. Schmelz, R. Rukwied, Tuning in C-nociceptors to reveal mechanisms in
906 chronic neuropathic pain. *Annals of Neurology* **83**, 945–957 (2018).
- 907 14. R. Schmidt, M. Schmelz, C. Forster, M. Ringkamp, E. Torebjörk, H. Handwerker, Novel classes of responsive
908 and unresponsive C nociceptors in human skin. *J Neurosci* **15**, 333–341 (1995).
- 909 15. C. Weidner, M. Schmelz, R. Schmidt, B. Hansson, H. O. Handwerker, H. E. Torebjörk, Functional attributes
910 discriminating mechano-insensitive and mechano-responsive C nociceptors in human skin. *J. Neurosci.* **19**, 10184–
911 10190 (1999).
- 912 16. F. Werland, M. Hirth, R. Rukwied, M. Ringkamp, B. Turnquist, E. Jorum, B. Namer, M. Schmelz, O. Obreja,
913 Maximum axonal following frequency separates classes of cutaneous unmyelinated nociceptors in the pig. *The
914 Journal of Physiology* **599**, 1595–1610 (2021).

- 915 17. V. Prato, F. J. Taberner, J. R. F. Hockley, G. Callejo, A. Arcourt, B. Tazir, L. Hammer, P. Schad, P. A.
916 Heppenstall, E. S. Smith, S. G. Lechner, Functional and Molecular Characterization of Mechanoinensitive “Silent”
917 Nociceptors. *Cell Rep* **21**, 3102–3115 (2017).
- 918 18. M. Kress, M. Koltzenburg, P. W. Reeh, H. O. Handwerker, Responsiveness and functional attributes of
919 electrically localized terminals of cutaneous C-fibers in vivo and in vitro. *J Neurophysiol* **68**, 581–595 (1992).
- 920 19. H. O. Handwerker, S. Kilo, P. W. Reeh, Unresponsive afferent nerve fibres in the sural nerve of the rat. *J*
921 *Physiol* **435**, 229–242 (1991).
- 922 20. S. J. Middleton, A. M. Barry, M. Comini, Y. Li, P. R. Ray, S. Shiers, A. C. Themistocleous, M. L. Uhelski, X.
923 Yang, P. M. Dougherty, T. J. Price, D. L. Bennett, Studying human nociceptors: from fundamentals to clinic. *Brain*
924 **144**, 1312–1335 (2021).
- 925 21. B. Lynn, K. Faulstroh, F. K. Pierau, The classification and properties of nociceptive afferent units from the skin
926 of the anaesthetized pig. *Eur J Neurosci* **7**, 431–437 (1995).
- 927 22. O. Obreja, M. Ringkamp, B. Namer, E. Forsch, A. Klusch, R. Rukwied, M. Petersen, M. Schmelz, Patterns of
928 activity-dependent conduction velocity changes differentiate classes of unmyelinated mechano-insensitive afferents
929 including cold nociceptors, in pig and in human. *Pain* **148**, 59–69 (2010).
- 930 23. A. K. Becker, A. Babes, M. M. Düll, M. Khalil, Z. Kender, J. Gröner, B. Namer, P. W. Reeh, S. K. Sauer,
931 Spontaneous activity of specific C-nociceptor subtypes from diabetic patients and mice: Involvement of reactive
932 dicarbonyl compounds and (sensitized) transient receptor potential channel A1. *J Peripher Nerv Syst* **28**, 202–225
933 (2023).
- 934 24. R. Jonas, V. Prato, S. G. Lechner, G. Groen, O. Obreja, F. Werland, R. Rukwied, A. Klusch, M. Petersen, R. W.
935 Carr, M. Schmelz, TTX-Resistant Sodium Channels Functionally Separate Silent From Polymodal C-nociceptors.
936 *Front. Cell. Neurosci.* **14** (2020), doi:10.3389/fncel.2020.00013.
- 937 25. M. Jung, M. Dourado, J. Maksymetz, A. Jacobson, B. I. Laufer, M. Baca, O. Foreman, D. H. Hackos, L. Riol-
938 Blanco, J. S. Kaminker, Cross-species transcriptomic atlas of dorsal root ganglia reveals species-specific programs
939 for sensory function. *Nat Commun* **14**, 366 (2023).
- 940 26. J. Kupari, D. Usoskin, M. Parisien, D. Lou, Y. Hu, M. Fatt, P. Lönnberg, M. Spångberg, B. Eriksson, N.
941 Barkas, P. V. Kharchenko, K. Loré, S. Khouri, L. Diatchenko, P. Ernfors, Single cell transcriptomics of primate
942 sensory neurons identifies cell types associated with chronic pain. *Nat Commun* **12**, 1510 (2021).
- 943 27. M. Q. Nguyen, L. J. von Buchholtz, A. N. Reker, N. J. P. Ryba, S. Davidson, *Single nucleus transcriptomic*
944 *analysis of human dorsal root ganglion neurons* (2021);
945 <https://www.biorxiv.org/content/10.1101/2021.07.02.450845v1>, p. 2021.07.02.450845.
- 946 28. N. Sharma, K. Flaherty, K. Lezgiyeva, D. E. Wagner, A. M. Klein, D. D. Ginty, The emergence of
947 transcriptional identity in somatosensory neurons. *Nature* **577**, 392–398 (2020).
- 948 29. D. Tavares-Ferreira, S. Shiers, P. R. Ray, A. Wangzhou, V. Jeevakumar, I. Sankaranarayanan, A. M. Cervantes,
949 J. C. Reese, A. Chamesian, B. A. Copits, P. M. Dougherty, R. W. Gereau, M. D. Burton, G. Dussor, T. J. Price,
950 Spatial transcriptomics of dorsal root ganglia identifies molecular signatures of human nociceptors. *Sci Transl Med*
951 **14**, eabj8186 (2022).
- 952 30. D. Usoskin, A. Furlan, S. Islam, H. Abdo, P. Lönnberg, D. Lou, J. Hjerling-Leffler, J. Haeggström, O.
953 Kharchenko, P. V. Kharchenko, S. Linnarsson, P. Ernfors, Unbiased classification of sensory neuron types by large-
954 scale single-cell RNA sequencing. *Nat. Neurosci.* **18**, 145–153 (2015).

- 955 31. J. Körner, A. Lampert, Functional subgroups of rat and human sensory neurons: a systematic review of
956 electrophysiological properties. *Pflugers Arch* **474**, 367–385 (2022).
- 957 32. C. R. Cadwell, A. Palasantza, X. Jiang, P. Berens, Q. Deng, M. Yilmaz, J. Reimer, S. Shen, M. Bethge, K. F.
958 Tolias, R. Sandberg, A. S. Tolias, Electrophysiological, transcriptomic and morphologic profiling of single neurons
959 using Patch-seq. *Nature Biotechnology* **34**, 199–203 (2016).
- 960 33. N. W. Gouwens, S. A. Sorensen, F. Baftizadeh, A. Budzillo, B. R. Lee, T. Jarsky, L. Alfiler, K. Baker, E.
961 Barkan, K. Berry, D. Bertagnolli, K. Bickley, J. Bomben, T. Braun, K. Brouner, T. Casper, K. Crichton, T. L.
962 Daigle, R. Dalley, R. A. de Frates, N. Dee, T. Desta, S. D. Lee, N. Dotson, T. Egger, L. Ellingwood, R. Enstrom, L.
963 Esposito, C. Farrell, D. Feng, O. Fong, R. Gala, C. Gamlin, A. Gary, A. Glandon, J. Goldy, M. Gorham, L.
964 Graybuck, H. Gu, K. Hadley, M. J. Hawrylycz, A. M. Henry, D. Hill, M. Hupp, S. Kebede, T. K. Kim, L. Kim, M.
965 Kroll, C. Lee, K. E. Link, M. Mallory, R. Mann, M. Maxwell, M. McGraw, D. McMillen, A. Mukora, L. Ng, L. Ng,
966 K. Ngo, P. R. Nicovich, A. Oldre, D. Park, H. Peng, O. Penn, T. Pham, A. Pom, Z. Popović, L. Potekhina, R.
967 Rajanbabu, S. Ransford, D. Reid, C. Rimorin, M. Robertson, K. Ronellenfitch, A. Ruiz, D. Sandman, K. Smith, J.
968 Sulc, S. M. Sunkin, A. Szafer, M. Tieu, A. Torkelson, J. Trinh, H. Tung, W. Wakeman, K. Ward, G. Williams, Z.
969 Zhou, J. T. Ting, A. Arkhipov, U. Sümbül, E. S. Lein, C. Koch, Z. Yao, B. Tasic, J. Berg, G. J. Murphy, H. Zeng,
970 Integrated Morphoelectric and Transcriptomic Classification of Cortical GABAergic Cells. *Cell* **183**, 935–953.e19
971 (2020).
- 972 34. M. Lipovsek, C. Bardy, C. R. Cadwell, K. Hadley, D. Kobak, S. J. Tripathy, Patch-seq: Past, Present, and
973 Future. *J Neurosci* **41**, 937–946 (2021).
- 974 35. F. Scala, D. Kobak, S. Shan, Y. Bernaerts, S. Latus, C. R. Cadwell, L. Hartmanis, E. Froudarakis, J. R.
975 Castro, Z. H. Tan, S. Papadopoulos, S. S. Patel, R. Sandberg, P. Berens, X. Jiang, A. S. Tolias, Layer 4 of mouse
976 neocortex differs in cell types and circuit organization between sensory areas. *Nature Communications* **10**, 4174
977 (2019).
- 978 36. L. Qi, M. Iskols, D. Shi, P. Reddy, C. Walker, K. Lezgiyeva, T. Voisin, M. Pawlak, V. K. Kuchroo, I. M. Chiu,
979 D. D. Ginty, N. Sharma, A mouse DRG genetic toolkit reveals morphological and physiological diversity of
980 somatosensory neuron subtypes. *Cell* **187**, 1508–1526.e16 (2024).
- 981 37. T. Parpaite, L. Brosse, N. Séjourné, A. Laur, Y. Mechoulah, P. Delmas, B. Coste, Patch-seq of mouse DRG
982 neurons reveals candidate genes for specific mechanosensory functions. *Cell Rep* **37**, 109914 (2021).
- 983 38. A.-H. Pool, H. Poldsam, S. Chen, M. Thomson, Y. Oka, Enhanced recovery of single-cell RNA-sequencing
984 reads for missing gene expression data, 2022.04.26.489449 (2022).
- 985 39. W. Renhal, I. Tochitsky, L. Yang, Y.-C. Cheng, E. Li, R. Kawaguchi, D. H. Geschwind, C. J. Woolf,
986 Transcriptional Reprogramming of Distinct Peripheral Sensory Neuron Subtypes after Axonal Injury. *Neuron* **108**,
987 128–144.e9 (2020).
- 988 40. A. Wangzhou, L. A. McIlvried, C. Paige, P. Barragan-Iglesias, S. Shiers, A. Ahmad, C. A. Guzman, G. Dussor,
989 P. R. Ray, R. W. Gereau, T. J. Price, Pharmacological target-focused transcriptomic analysis of native vs cultured
990 human and mouse dorsal root ganglia. *Pain* **161**, 1497–1517 (2020).
- 991 41. S. A. Bhuiyan, M. Xu, L. Yang, E. Semizoglou, P. Bhatia, K. I. Pantaleo, I. Tochitsky, A. Jain, B. Erdogan, S.
992 Blair, V. Cat, J. M. Mwirigi, I. Sankaranarayanan, D. Tavares-Ferreira, U. Green, L. A. McIlvried, B. A. Copits, Z.
993 Bertels, J. S. Del Rosario, A. J. Widman, R. A. Slivicki, J. Yi, R. Sharif-Naeini, C. J. Woolf, J. K. Lennerz, J. L.
994 Whited, T. J. Price, null Robert W Gereau Iv, W. Renhal, Harmonized cross-species cell atlases of trigeminal and
995 dorsal root ganglia. *Sci Adv* **10**, ead9173 (2024).
- 996 42. A. Snape, J. F. Pittaway, M. D. Baker, Excitability parameters and sensitivity to anemone toxin ATX-II in rat
997 small diameter primary sensory neurones discriminated by Griffonia simplicifolia isolectin IB4. *The Journal of
998 Physiology* **588**, 125–137 (2010).

- 999 43. P. A. Köster, E. Leipold, J. Tigerholm, A. Maxion, B. Namer, T. Stiehl, A. Lampert, Sodium channels expressed
1000 in nociceptors contribute distinctly to action potential subthreshold phase, upstroke and shoulder,
1001 2023.09.03.556095 (2024).
- 1002 44. M. Schmelz, K. Michael, C. Weidner, R. Schmidt, H. E. Torebjörk, H. O. Handwerker, Which nerve fibers
1003 mediate the axon reflex flare in human skin? *Neuroreport* **11**, 645–648 (2000).
- 1004 45. X. Cheng, J.-S. Choi, S. G. Waxman, S. D. Dib-Hajj, Mini-review - Sodium channels and beyond in peripheral
1005 nerve disease: Modulation by cytokines and their effector protein kinases. *Neurosci Lett* **741**, 135446 (2021).
- 1006 46. M. D. Baker, M. A. Nassar, Painful and painless mutations of SCN9A and SCN11A voltage-gated sodium
1007 channels. *Pflugers Arch* **472**, 865–880 (2020).
- 1008 47. G. Goodwin, S. B. McMahon, The physiological function of different voltage-gated sodium channels in pain.
1009 *Nat Rev Neurosci* (2021), doi:10.1038/s41583-021-00444-w.
- 1010 48. J. B. Levy, C. Schindler, R. Raz, D. E. Levy, R. Baron, M. C. Horowitz, Activation of the JAK-STAT signal
1011 transduction pathway by oncostatin-M cultured human and mouse osteoblastic cells. *Endocrinology* **137**, 1159–1165
1012 (1996).
- 1013 49. S. G. Kwatra, Z. A. Bordeaux, V. Parthasarathy, A. L. Kollhoff, A. Alajmi, T. Pritchard, H. L. Cornman, A.
1014 Kambala, K. K. Lee, J. Manjunath, E. Z. Ma, C. Dillen, M. M. Kwatra, Efficacy and Safety of Abrocitinib in
1015 Prurigo Nodularis and Chronic Pruritus of Unknown Origin: A Nonrandomized Controlled Trial. *JAMA
Dermatology* **160**, 717–724 (2024).
- 1017 50. Z. Szekanecz, M. H. Buch, C. Charles-Schoeman, J. Galloway, G. A. Karpouzas, L. E. Kristensen, S. R.
1018 Ytterberg, A. Hamar, R. Fleischmann, Efficacy and safety of JAK inhibitors in rheumatoid arthritis: update for the
1019 practising clinician. *Nat Rev Rheumatol* **20**, 101–115 (2024).
- 1020 51. Y. Tanaka, Y. Luo, J. J. O’Shea, S. Nakayamada, Janus kinase-targeting therapies in rheumatology: a
1021 mechanisms-based approach. *Nat Rev Rheumatol* **18**, 133–145 (2022).
- 1022 52. T. Bishop, A. Ballard, H. Holmes, A. R. Young, S. B. McMahon, Ultraviolet-B induced inflammation of human
1023 skin: characterisation and comparison with traditional models of hyperalgesia. *Eur J Pain* **13**, 524–532 (2009).
- 1024 53. T. A. Nees, N. Wang, P. Adamek, N. Zeitzschel, C. Verkest, C. La Porta, I. Schaefer, J. Virnich, S. Balkaya, V.
1025 Prato, C. Morelli, V. Begay, Y. J. Lee, A. Tappe-Theodor, G. R. Lewin, P. A. Heppenstall, F. J. Taberner, S. G.
1026 Lechner, Role of TMEM100 in mechanically insensitive nociceptor un-silencing. *Nat Commun* **14**, 1899 (2023).
- 1027 54. T. Hoffmann, R. De Col, K. Messlinger, P. W. Reeh, C. Weidner, Mice and rats differ with respect to activity-
1028 dependent slowing of conduction velocity in the saphenous peripheral nerve. *Neurosci Lett* **592**, 12–16 (2015).
- 1029 55. C. Rostock, K. Schrenk-Siemens, J. Pohle, J. Siemens, Human vs. Mouse Nociceptors - Similarities and
1030 Differences. *Neuroscience* **387**, 13–27 (2018).
- 1031 56. B. Coste, J. Mathur, M. Schmidt, T. J. Earley, S. Ranade, M. J. Petrus, A. E. Dubin, A. Patapoutian, Piezo1 and
1032 Piezo2 are essential components of distinct mechanically activated cation channels. *Science* **330**, 55–60 (2010).
- 1033 57. L. Beaulieu-Laroche, M. Christin, A. Donoghue, F. Agosti, N. Yousefpour, H. Petitjean, A. Davidova, C.
1034 Stanton, U. Khan, C. Dietz, E. Faure, T. Fatima, A. MacPherson, S. Mouchbahani-Constance, D. G. Bisson, L.
1035 Haglund, J. A. Ouellet, L. S. Stone, J. Samson, M.-J. Smith, K. Ask, A. Ribeiro-da-Silva, R. Blunck, K. Poole, E.
1036 Bourinet, R. Sharif-Naeini, TACAN Is an Ion Channel Involved in Sensing Mechanical Pain. *Cell* **180**, 956–967.e17
1037 (2020).

- 1038 58. S. Chakrabarti, J. D. Klich, M. A. Khallaf, O. Sánchez-Carranza, Z. M. Baran, A. Rossi, A. T.-L. Huang, T.
1039 Pohl, R. Fleischer, C. Fürst, A. Hammes, V. Bégay, H. Hörnberg, K. Poole, G. R. Lewin, Touch sensation requires
1040 the mechanically-gated ion channel Elkin1, 2023.06.09.544247 (2023).
- 1041 59. L. Grohs, L. Cheng, S. Cönen, B. G. Haddad, A. Bülow, I. Toklucu, L. Ernst, J. Körner, G. Schmalzing, A.
1042 Lampert, J.-P. Machtens, R. Hausmann, Diclofenac and other non-steroidal anti-inflammatory drugs (NSAIDs) are
1043 competitive antagonists of the human P2X3 receptor. *Front Pharmacol* **14**, 1120360 (2023).
- 1044 60. M. Hirth, R. Rukwied, A. Gromann, B. Turnquist, B. Weinkauf, K. Francke, P. Albrecht, F. Rice, B. Hägglöf,
1045 M. Ringkamp, M. Engelhardt, C. Schultz, M. Schmelz, O. Obreja, Nerve growth factor induces sensitization of
1046 nociceptors without evidence for increased intraepidermal nerve fiber density. *Pain* **154**, 2500–2511 (2013).
- 1047 61. K. J. Ernst, K. Okonechnikov, J. Bageritz, J.-P. Mallm, A. Wittmann, K. K. Maaß, S. Leible, M. Boutros, S. M.
1048 Pfister, M. Zuckermann, D. T. W. Jones, Establishment of a simplified preparation method for single-nucleus RNA-
1049 sequencing and its application to long-term frozen tumor tissues, 2020.10.23.351809 (2020).
- 1050 62. L. Yang, I. Tochitsky, C. J. Woolf, W. Renthal, Isolation of Nuclei from Mouse Dorsal Root Ganglia for Single-
1051 nucleus Genomics. *Bio Protoc* **11**, e4102 (2021).
- 1052 63. C.-L. Li, K.-C. Li, D. Wu, Y. Chen, H. Luo, J.-R. Zhao, S.-S. Wang, M.-M. Sun, Y.-J. Lu, Y.-Q. Zhong, X.-Y.
1053 Hu, R. Hou, B.-B. Zhou, L. Bao, H.-S. Xiao, X. Zhang, Somatosensory neuron types identified by high-coverage
1054 single-cell RNA-sequencing and functional heterogeneity. *Cell Res* **26**, 83–102 (2016).
- 1055 64. M. Q. Nguyen, C. E. Le Pichon, N. Ryba, P. Mason, E. Marder, P. Mason, Eds. Stereotyped transcriptomic
1056 transformation of somatosensory neurons in response to injury. *eLife* **8**, e49679 (2019).
- 1057 65. M. Q. Nguyen, Y. Wu, L. S. Bonilla, L. J. von Buchholtz, N. J. P. Ryba, Diversity amongst trigeminal neurons
1058 revealed by high throughput single cell sequencing. *PLoS One* **12**, e0185543 (2017).
- 1059 66. A. Zeisel, H. Hochgerner, P. Lönnberg, A. Johnsson, F. Memic, J. van der Zwan, M. Häring, E. Braun, L. E.
1060 Borm, G. La Manno, S. Codeluppi, A. Furlan, K. Lee, N. Skene, K. D. Harris, J. Hjerling-Leffler, E. Arenas, P.
1061 Ernfors, U. Marklund, S. Linnarsson, Molecular Architecture of the Mouse Nervous System. *Cell* **174**, 999–
1062 1014.e22 (2018).
- 1063 67. S. Picelli, O. R. Faridani, A. K. Björklund, G. Winberg, S. Sagasser, R. Sandberg, Full-length RNA-seq from
1064 single cells using Smart-seq2. *Nat Protoc* **9**, 171–181 (2014).
- 1065 68. S. Fischer, M. Crow, B. D. Harris, J. Gillis, Scaling up reproducible research for single-cell transcriptomics
1066 using MetaNeighbor. *Nat Protoc* **16**, 4031–4067 (2021).
- 1067 69. M. Sekerli, C. A. Del Negro, R. H. Lee, R. J. Butera, Estimating action potential thresholds from neuronal time-
1068 series: new metrics and evaluation of methodologies. *IEEE Trans Biomed Eng* **51**, 1665–1672 (2004).
- 1069 70. B. Turnquist, M. Leverentz, E. Swanson, Neural spike classification using parallel selection of all algorithm
1070 parameters. *J Neurosci Methods* **137**, 291–298 (2004).
- 1071 71. A. H. Bretag, Synthetic interstitial fluid for isolated mammalian tissue. *Life Sciences* **8**, 319–329 (1969).
- 1072 72. M. Schmelz, C. Forster, R. Schmidt, M. Ringkamp, H. O. Handwerker, H. E. Torebjörk, Delayed responses to
1073 electrical stimuli reflect C-fiber responsiveness in human microneurography. *Exp Brain Res* **104**, 331–336 (1995).
- 1074
- 1075

1076 **Acknowledgments:**

1077 The authors thank the FlowCore and next generation sequencing core facilities of the Medical Faculty Mannheim at
1078 Heidelberg University for their assistance with nuclei sorting and generation of single-nucleus gene expression
1079 libraries and sequencing. We also thank Heidi Theis (PRECISE, DZNE, Bonn) for preparation of Patch-seq
1080 libraries. The authors thank the organ donors and their families for their enduring gift. The authors thank the
1081 Genome Center at The University of Texas at Dallas for the services to support pig DRG spatial sequencing.

1082

1083 **Funding:**

1084 Clinician Scientist program of the Faculty of Medicine of the RWTH Aachen university (JK)
1085 DFG, German Research Foundation 363055819/GRK2415 (AL)
1086 DFG, German Research Foundation 368482240/GRK2416 (AL)
1087 DFG, German Research Foundation LA 2740/6-1 (AL)
1088 DFG, German Research Foundation NA 970/5-1 (BN)
1089 DFG, German Research Foundation 255156212/CRC1158/Z02-INF (HJS)
1090 DFG, German Research Foundation 350193106/FOR2690/TP01 (HJS)
1091 DFG, German Research Foundation 255156212/SFB1158 A01 (MS)
1092 DFG, German Research Foundation 350193106/FOR2690 (MS)
1093 DFG, German Research Foundation 1587/10-1 (IK)
1094 DFG, German Research Foundation 1587/11-1 (IK)
1095 Interdisciplinary Center for Clinical Research within the Faculty of Medicine at the RWTH
1096 Aachen University IZKF TN1-1/IA 532001 (AL)
1097 CAMH Discovery Fund, Krembil Foundation, Kavli Foundation, McLaughlin Foundation,
1098 Natural Sciences and Engineering Research Council of Canada (RGPIN-2020-05834 and
1099 DGECR-2020-00048 (DH,ST)
1100 Canadian Institutes of Health Research (NGN-171423 and PJT-175254) (DH,ST)
1101 Simons Foundation Autism Research Initiative (DH,ST)
1102 Baden-Württemberg through bwHPC and the German Research Foundation (DFG) through
1103 grant INST 35/1597-1 FUGG (HJS, MS)
1104 NIH grant U19NS130608 (TJP)
1105 German Research Foundation (DFG) through grant INST 35/1503-1 FUGG (HJS,MS)
1106 Interdisciplinary Center for Clinical
1107 Research within the faculty of Medicine at the RWTH Aachen University (BN)
1108 NIH U19 NS130617, Rita Allen Foundation, Burroughs Wellcome Fund Career Award in
1109 Medical Sciences (WR)
1110

1111 **Author contributions:**

1112 Conceptualization: JK, DH, HJS, TJP, MS, BN, ST, AL.
1113 Methodology: JK, DH, HJS, MMM, NH, IT, MB, BN, ST, AL, TS.
1114 Software: JK, DH, MMM, DT, NNI, TS.
1115 Validation: JK, DH, HJS, ST, AL.
1116 Formal analysis: JK, DH, HJS, MMM, AF, DT, AM, SAB, BN.
1117 Investigation: JK, HJS, MMM, NH, AF, IT, RB, IS, DT, SS, AM, LB, JSS, IK, MS, BN, ST,
1118 TS.
1119 Resources: DT, LE, MB, BN, AL.
1120 Data Curation: JK, DH, HJS, MMM, AF, AM, MB, BN, ST, AL.
1121 Writing - Original Draft: JK, DH, MMM, TJP, ST, AL.
1122 Writing - Review & Editing: JK, DH, HJS, MMM, NH, AF, AM, LE, MB, IK, MS, SAB,
1123 WR, BN, ST, AL.
1124 Visualization: JK, DH, HJS, MMM, NH, ST.
1125 Supervision: MB, TJP, BN, ST, AL.
1126 Project administration: JK, HJS, MB, NH, TJP, ST, AL.
1127 Funding acquisition: JK, HJS, IK, WR, TJP, BN, AL.

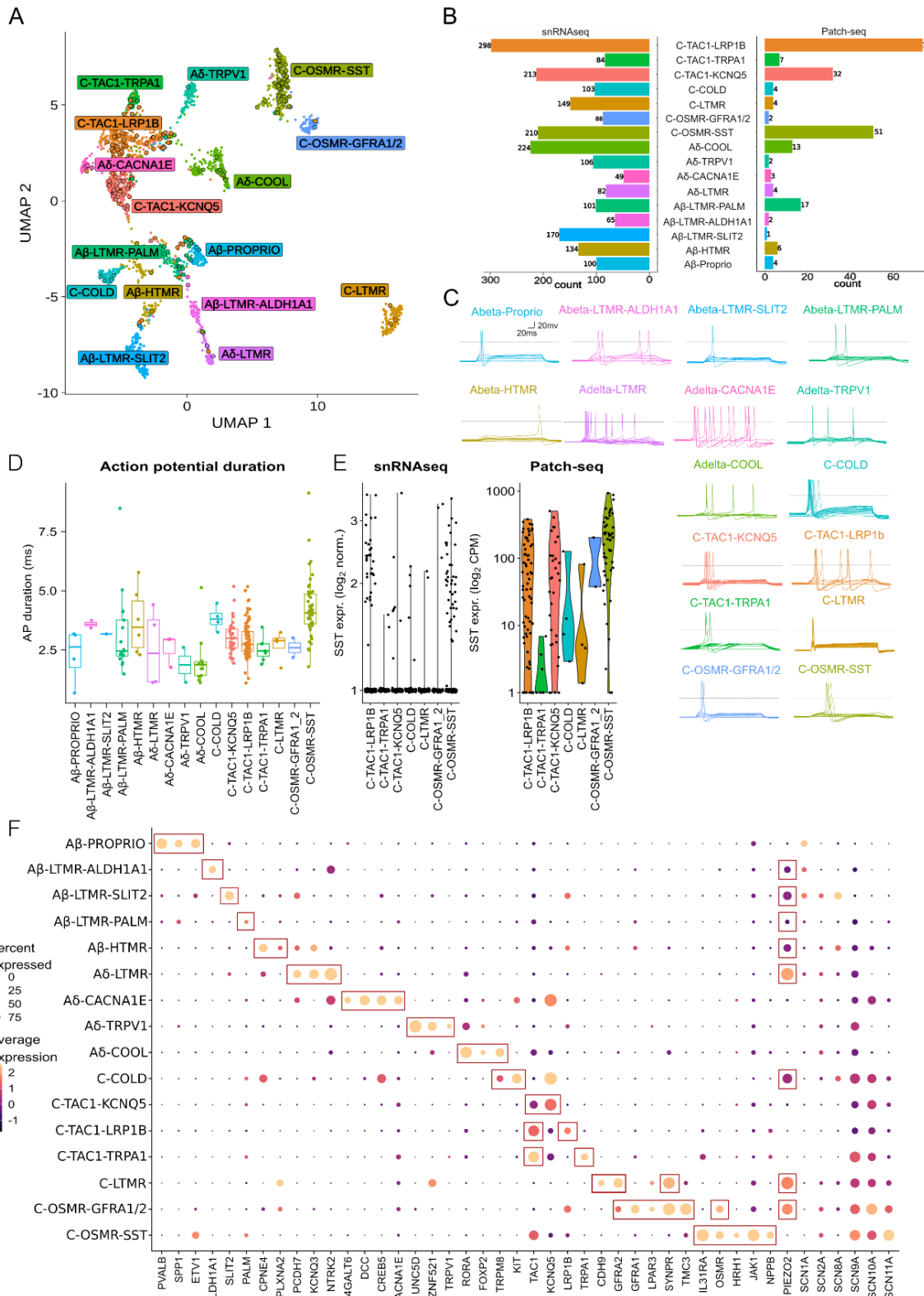
1128 **Competing interests:**

1129 AL and TJP receive counselling fees from and had research contracts with Grünenthal. WR
1130 received counseling fees from Grunenthal and has a research contract from Pfizer. Parts of the
1131 data in the manuscript (Costs for consumables, services and salary for sequencing Visium spatial
1132 transcriptomics and parts of the PatchSeq experiments) were generated within a research contract
1133 with Grünenthal. BN has a counselling contract with Vertex. All other authors declare that they
1134 have no competing interests.

1135 **Data and materials availability:**

1136 All raw gene expression data with detailed metadata supporting the findings of this study will be
1137 openly after peer-reviewed publication.
1138 Integration and analysis code, as well as extracted patch recording features will be available after
1139 peer-reviewed publication.
1140

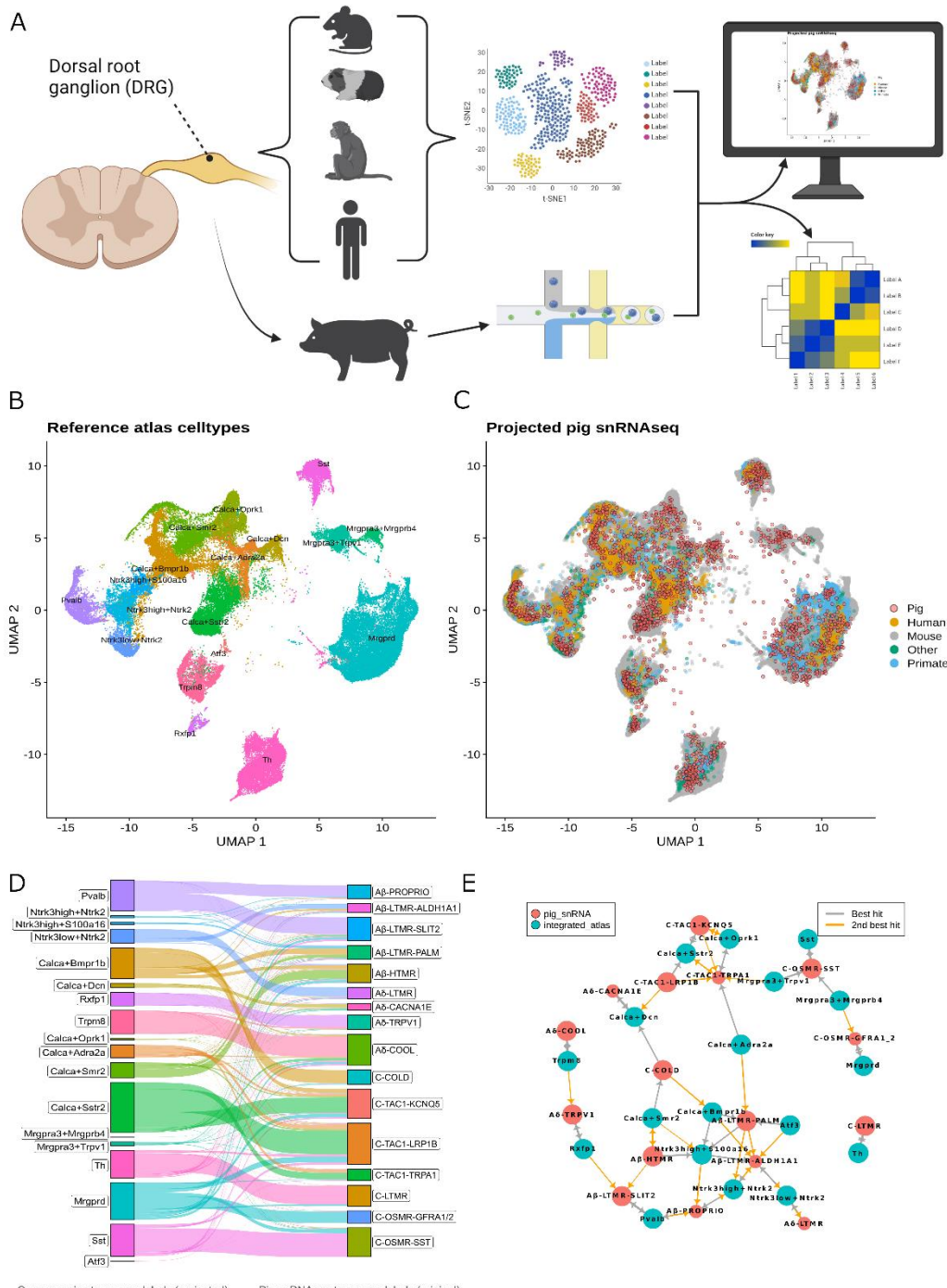
1141 **Figures**



1143 **Figure 1: A multi-modal taxonomy of pig dorsal root ganglion neurons**

1144
1145 (A) Multi-modal neuronal taxonomy of porcine DRG, displaying DRG neuronal subtypes categorized by multi-
1146 variate gene expression profiles from snRNAseq (small dots) and Patch-seq (larger circles). Colours indicate
1147 neuronal identity based on unbiased clustering of snRNAseq data. (B) Overall counts of cells in each neuronal
1148 subtype from snRNAseq (left) and Patch-seq (right). C) Representative current-clamp voltage traces for exemplar
1149 cells characterized via Patch-seq for each cell type in A). Voltage trace shows an overlay of 200 ms rectangular
1150 depolarizing pulses of increasing intensities. Scale bar insets represent 20 ms (horizontal) and 20 mV (vertical).
1151 Dashed line indicates 0 mv. (D) Distributions of action potential duration (C-fibers: 3.34 ± 0.082 ms, A-fibers: 2.75
1152 ± 0.196 ms, $p=8.88 \times 10^{-5}$, two-sided Wilcoxon rank-sum test. Longest AP duration for C-OSMR-SST: 4.26 ± 0.170
1153 ms, $p = 6.69 \times 10^{-11}$, two-sided Kruskal-Wallis test for each neuronal subtype (mean \pm SEM). (E) SST expression in
1154 snRNAseq (left) and Patch-seq (right). Each point represents a single cell, with expression quantified by RNA-seq
1155 read counts and displayed on a log-transformed y-axis for snRNAseq (left) and Patch-seq (right). Difference in units
1156 between axes related to technology differences. (F) Group dot plot illustrating snRNAseq-based expression of
1157 specific genes for each neuronal subtype. Inset boxes reflect representative markers or cell type-relevant genes
1158 discussed in the text.
1159
1160
1161
1162

1163
1164



1165

1166 **Figure 2: High concordance between pig and cross species neuronal taxonomies**

1167 (A) Schematic overview of the workflow to compare pig and cross-species neuronal taxonomies. (B) UMAP
1168 visualization of cell types in the cross-species DRG atlas, with each cluster (colors) representing a distinct DRG
1169 neuron cell type. (C) Projection of pig snRNA-seq cells (red dots) onto the cross-species atlas (same as A, cells
1170 colored by species of dataset origin). (D) River plot illustrating the cell type correspondence of pig snRNAseq cells

1171 after projecting into cross-species taxonomy (left) and original pig snRNA-seq taxonomy labels (right, cell type
1172 colors same as in Figure 1). Width of connecting line strips indicates the count of pig snRNAseq cells mapping
1173 between categories. (E) MetaNeighbor cluster graph visualization showing the relationship between pig snRNA-seq
1174 cell types (red nodes) and cross-species taxonomy cell types (blue nodes). Edges represent strong similarities
1175 between cell types, with thicker edges indicating stronger associations. Best hits (grey lines) indicate closest cell
1176 types by co-expression whereas 2nd best hit (orange lines) indicates second closest cell type.
1177

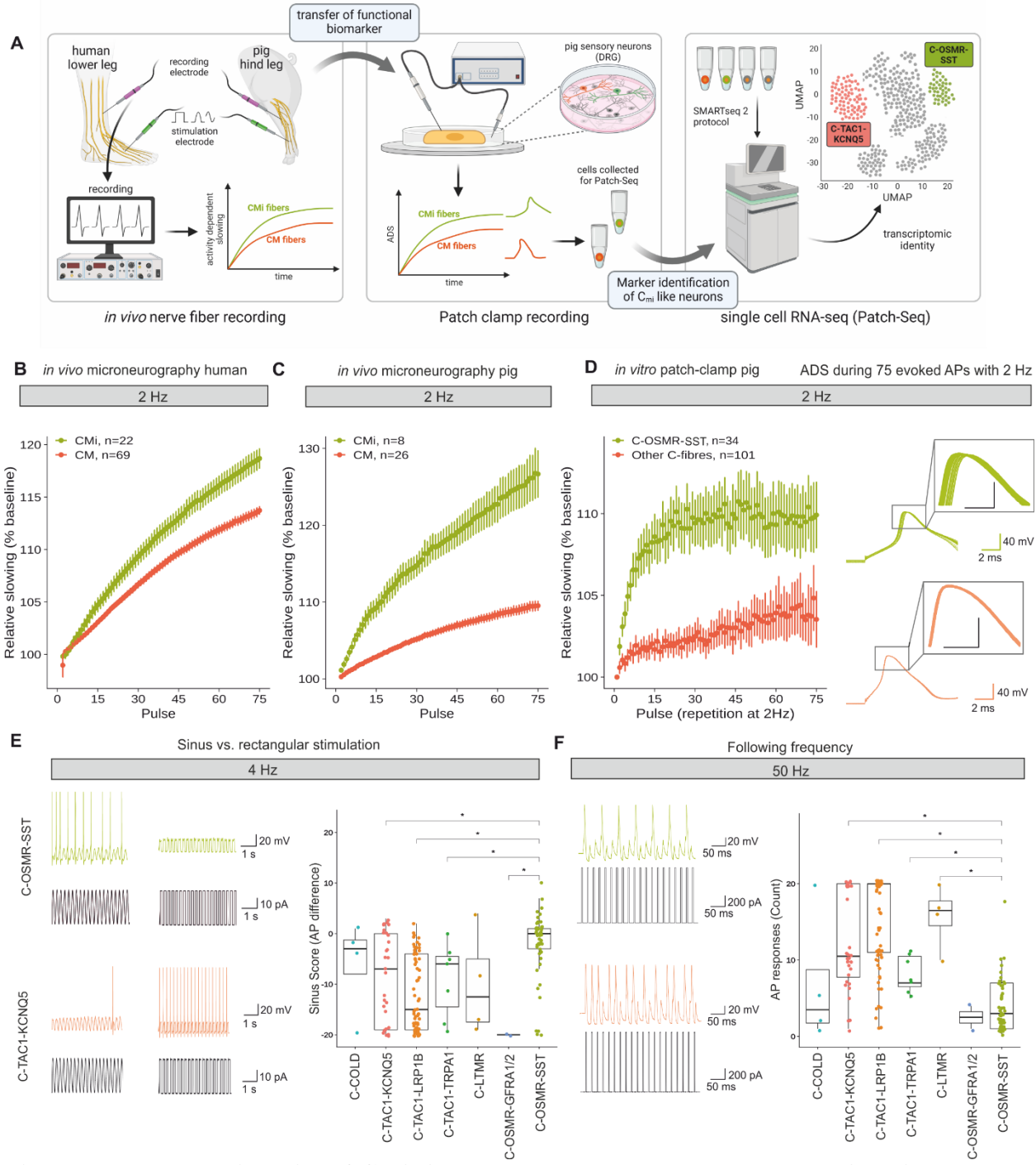
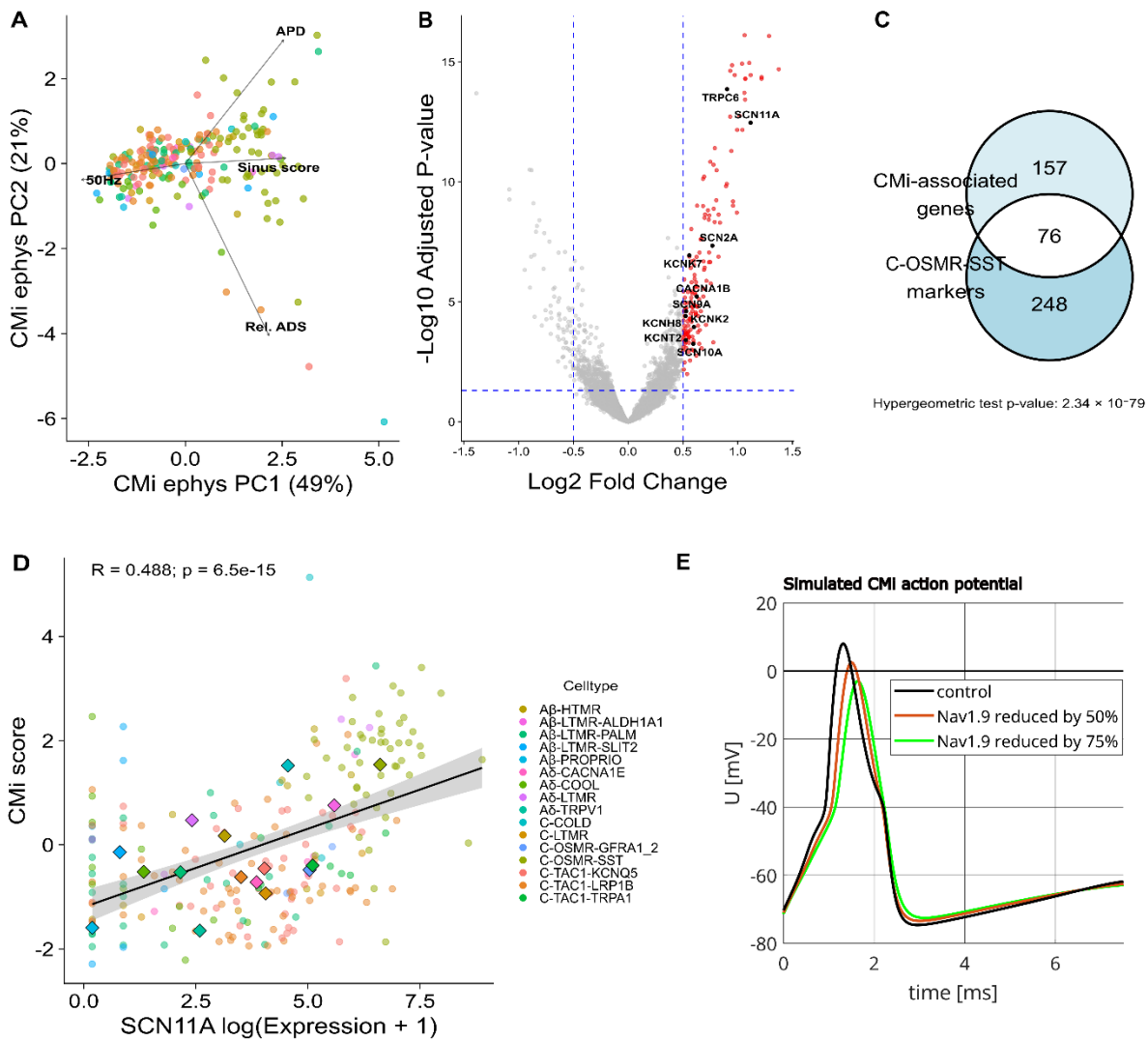


Figure 3: Molecular identity of CMIs in Patch-seq and adapted electrophysiological stimulation protocols in vitro

(A) Schematic for identifying molecular markers of mechano-insensitive C-fibers (CMis). CMis are traditionally identified *in vivo* using electrical stimulation protocols applied to the skin (left panel). Functional biomarkers of CMis include activity dependent slowing (ADS) upon repetitive stimulation, observed in CMis but not mechanosensitive C-fibers (CMs). We transferred these CMi-discriminating functional biomarkers into electrophysiological stimulation protocols that can be applied to DRG neurons using Patch clamp recordings *in vitro* (middle panel). This enables identifying molecular markers of putative CMi-like neurons using transcriptomics from

1188 Patch-seq (right panel). **(B,C)** *In vivo* characterization of ADS (y-axis) relative to stimulation pulse number (x-axis)
 1189 for CMi-fibers (green) and polymodal CMs (red) in humans (B) and pigs (C). **(D)** Similar to B,C), showing ADS
 1190 from Patch-seq characterized neurons stimulated using somatic current injection. Cells colored by molecular cell
 1191 type, highlighting differences between C-OSMR-SST cells (green, $110 \pm 2.04\%$, n=34) compared to all other C-
 1192 fiber neurons in Patch-seq dataset (red, $104 \pm 1.73\%$, n=110, $p = 9.27 \times 10^{-7}$, Mann-Whitney U = 741.5). Right panel
 1193 shows overlay of 75 APs induced by 1 nA current injection for 10 ms delivered at 2 Hz from an example C-OSMR-
 1194 SST (top) and C-TAC1-KCNQ5 neuron (bottom). Note that APs become more delayed over the course of the
 1195 stimulation protocol, especially in the C-OSMR-SST neurons, but comparatively less so in the C-TAC1-KCNQ5
 1196 neurons. **(E)** Left, Representative voltage trace (top) and current stimulation (bottom) traces evoked by sinusoidal
 1197 (left) versus rectangular stimulation (right). Right, Quantification of neuronal sinus scores across C-fiber neurons
 1198 characterized via Patch-seq. Sinus scores are defined as the difference in AP count evoked between sinusoidal
 1199 versus rectangular stimuli; positive scores indicate greater CMi-like activity. ANOVA ($F(6, 158) = 9.03$, $p <$
 1200 0.00001. **(F)** Left, Illustration of calculation of following frequency, where neurons are stimulated with 20 1nA
 1201 current pulses for 4 ms at 50 Hz. Right, count of AP responses evoked by 50 Hz stimuli designed to assess efficacy
 1202 to follow high frequency stimuli; fewer evoked APs indicate greater CMi-like activity. Asterisks denote statistical
 1203 significance with $p < 0.05$ as determined by an ANOVA ($F(6, 166) = 24.59$, $p < 0.0001$) followed by Tukey's post-
 1204 hoc HSD test.
 1205
 1206

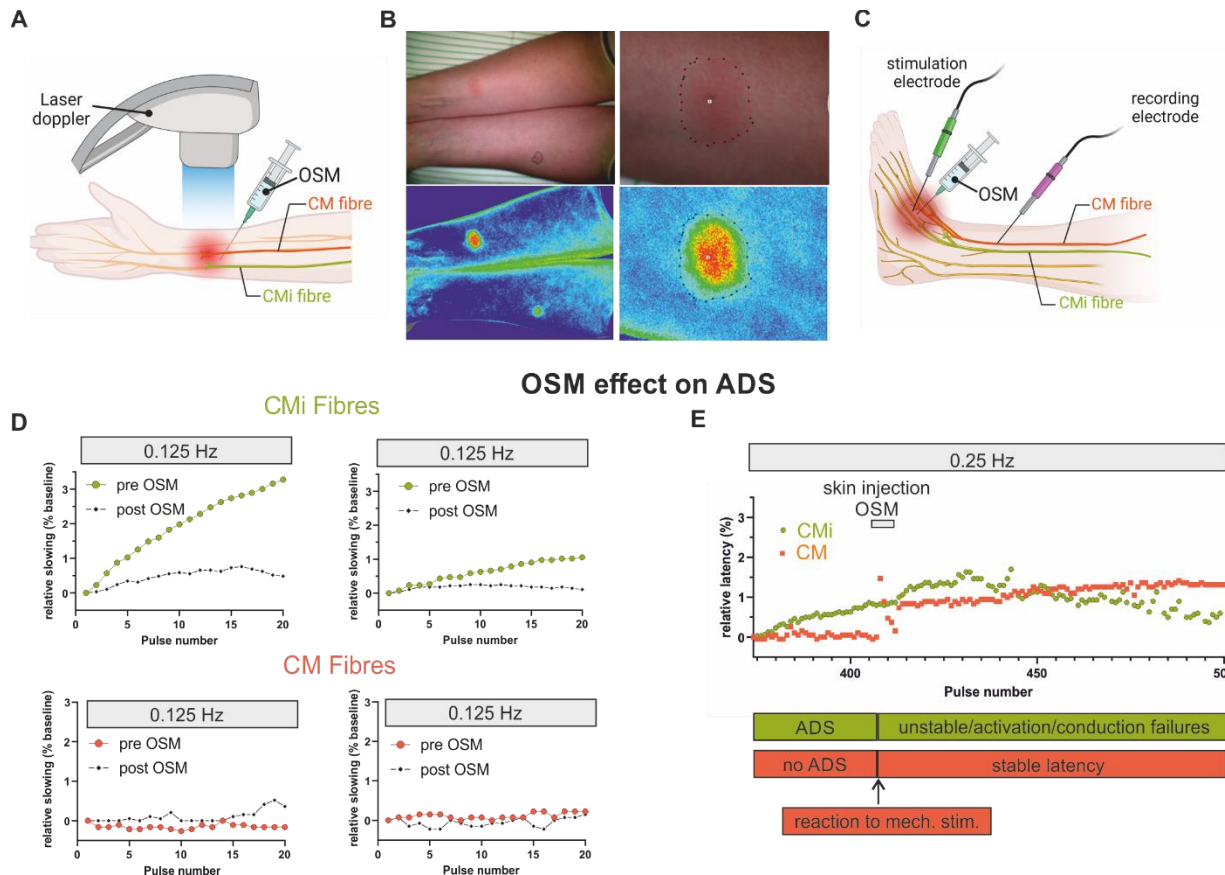


1207
 1208

1209 **Figure 4: Electrophysiological feature guided analysis of genes associated with CMi
1210 phenotype**

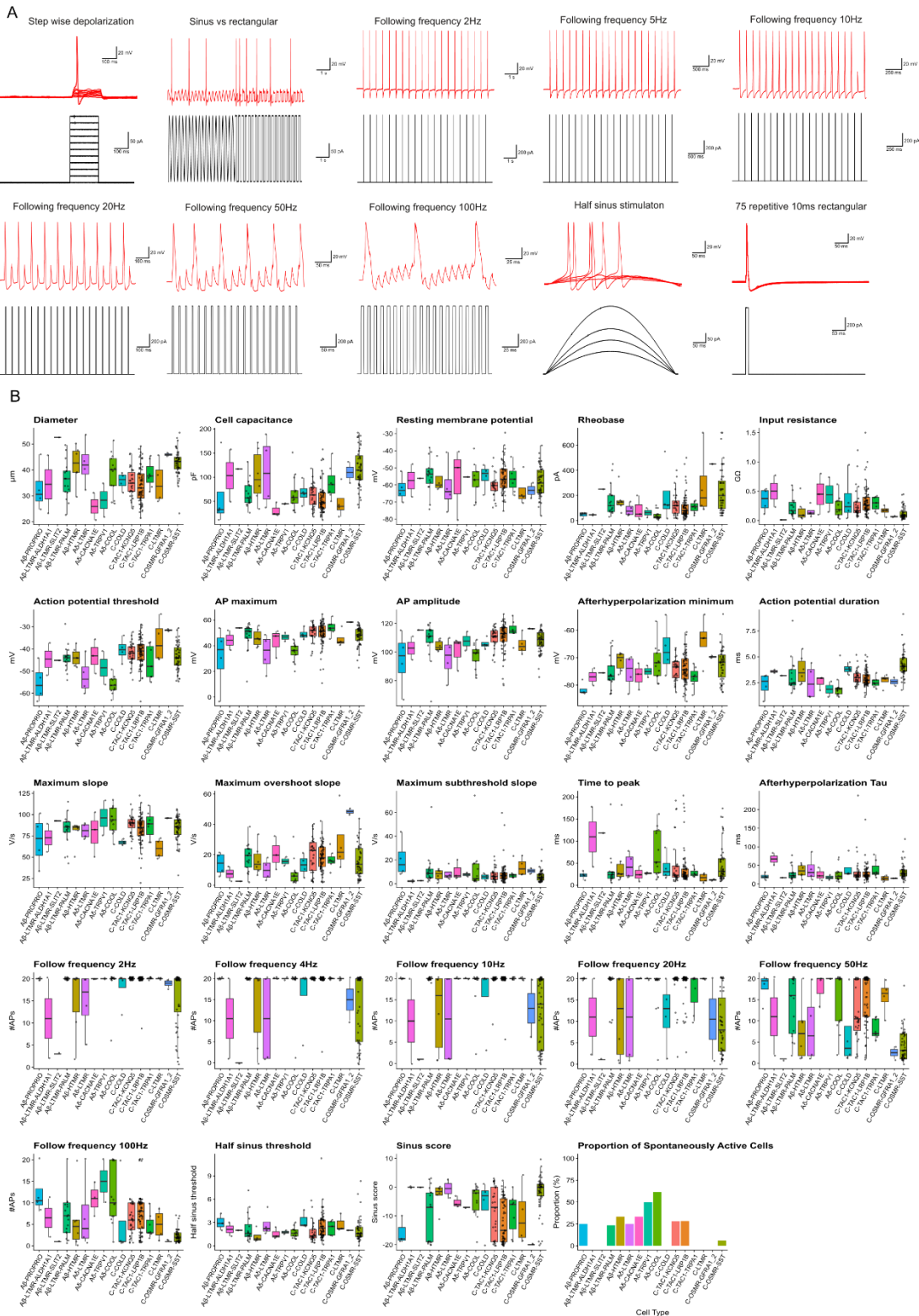
1211 (A) PCA biplot of CMi-related electrophysiology features. Each point represents a single neuron, colored by cell
1212 type. Arrows indicate the contribution of each electrophysiological feature to the principal components. (B) Volcano
1213 plot showing CMi score-associated genes. Axes indicate magnitude (x-axis) and statistical significance (y-axis) of
1214 association between gene expression and CMi score. Red dots indicate significantly differentially expressed genes
1215 (adjusted p-value < 0.05 and log₂ fold change > 0.5). Black dots highlight ion channel genes. Vertical blue dashed
1216 lines indicate log₂ fold change thresholds, and the horizontal blue dashed line indicates the adjusted p-value
1217 threshold. (C) Venn diagram illustrating the overlap between CMi-associated genes (red genes highlighted in B) and
1218 C-OOSMR-SST markers (derived from snRNA-seq data). (D) Correlation between SCN11A expression and CMi
1219 score. Each point represents a single neuron, colored by cell type. Larger diamond-shaped points indicate the mean
1220 expression and CMi score for each cell type. The black line shows linear regression fit with 95% confidence
1221 interval. (E) Simulated action potential waveforms demonstrating the effect of reducing Nav1.9 (SCN11A)
1222 conductance. Black trace shows control condition, while red and green traces show the effects of 50% and 75%
1223 reductions in Nav1.9 conductance, respectively, illustrating the channel's contribution to action potential
1224 characteristics.

1225



1226
1227 **Figure 5: Applying OSM in humans in vivo selectively affects CMi fibers**

1228
1229 (A) Schematic illustrating the use of oncostatin-M (OSM) during human superficial blood flow measurements. (B)
1230 Injection of OSM induces an axon reflex erythema of $275 \pm 108.3 \text{ mm}^2$ ($n=4$) in human skin after 24 h. Images show
1231 superficial blood flow (lower) and corresponding photographs (upper) of one participant's forearms at 24 h after
1232 injection (500 ng right distal, 250 ng left proximal). Lower panels show close-ups of injection site in right arm. (C)
1233 Schematic illustrating the use of oncostatin-M (OSM) during human microneurography experiments. OSM and
1234 electrical stimulation are applied to C-fiber nerve endings while AP responses of corresponding C-fiber axon(s) to
1235 the constant low frequency electrical stimulation are recorded simultaneously. (D) Microneurography recordings of
1236 two CMi- and two CM-fibers before (large colored circles) and 7 min after injection of 500 ng OSM (small black
1237 markers). Y-axis indicates differences in ADS as change in relative AP latency following delivery of 0.125 Hz test
1238 pulses. Following application of OSM, characteristic ADS is abolished in CMis but no change in ADS is observed
1239 in CMs. (E) Microneurography recordings of a CMi- (green) and CM-fiber (orange) before and after intraepidermal
1240 OSM injection during repetitive stimulation with 0.25 Hz. Subsequent response latencies of electrically induced APs
1241 are shown normalized to baseline latency determined before pulse 374. The CMi-fiber undergoes ADS during initial
1242 pulses. The CM fiber is mechanically activated by injection, as seen by a sudden latency increase followed by
1243 normalisation, and afterwards, ADS is stable. In contrast, the mechano-insensitive CMi-fiber is not activated by the
1244 mechanical aspect of injection but shows unstable latency afterwards. Some of these instabilities may be occurrence
1245 of spurious OSM induced discharges and numerous conduction failures following OSM injection, demonstrating an
1246 affection of CMi- but not CM-fibers by OSM injection.
1247



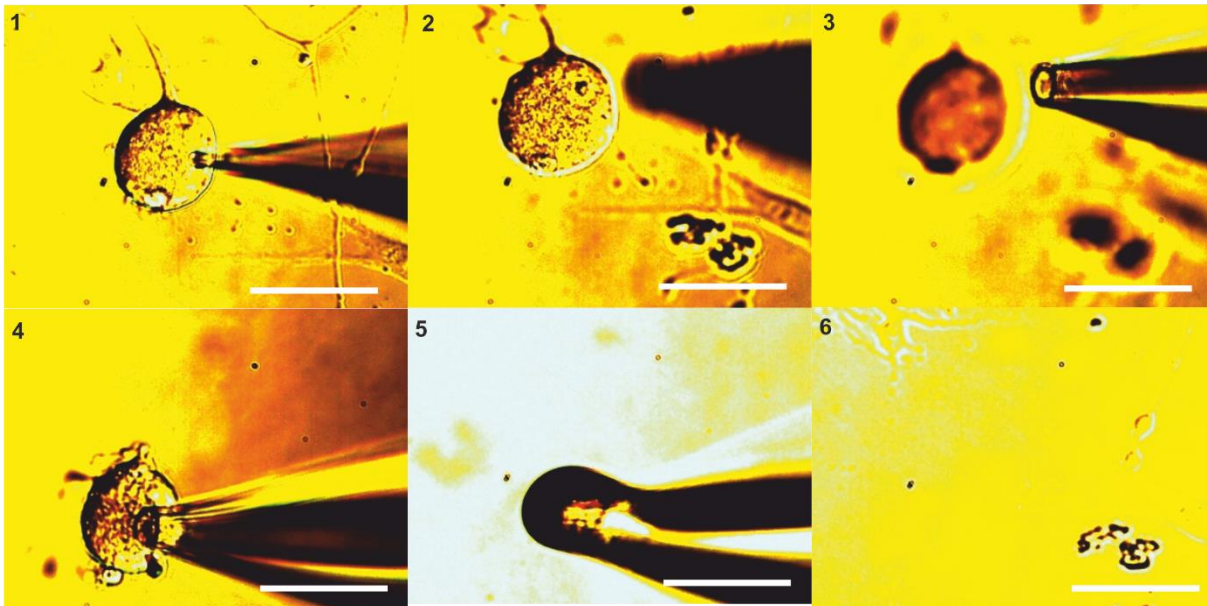
1248

1249 **Figure S1: Extended electrophysiological data**

1250
1251
1252
1253
1254
1255

A) Pulse protocols (black) for electrophysiological assessment and example patch-clamp recording traces of pig DRGs (red). From up left to down right: 200 ms stepwise depolarization protocol, sine vs rectangular 4 Hz stimulation, 20 1 nA pulses at 2, 5, 10, 20, 50 and 100 Hz, 500 ms half sine-shaped stimulation, 75 repetitive 1 nA 10 ms stimulations. **B)** Combined scatter and boxplots showing quantification of each electrophysiological feature per mapped transcriptomic identity.

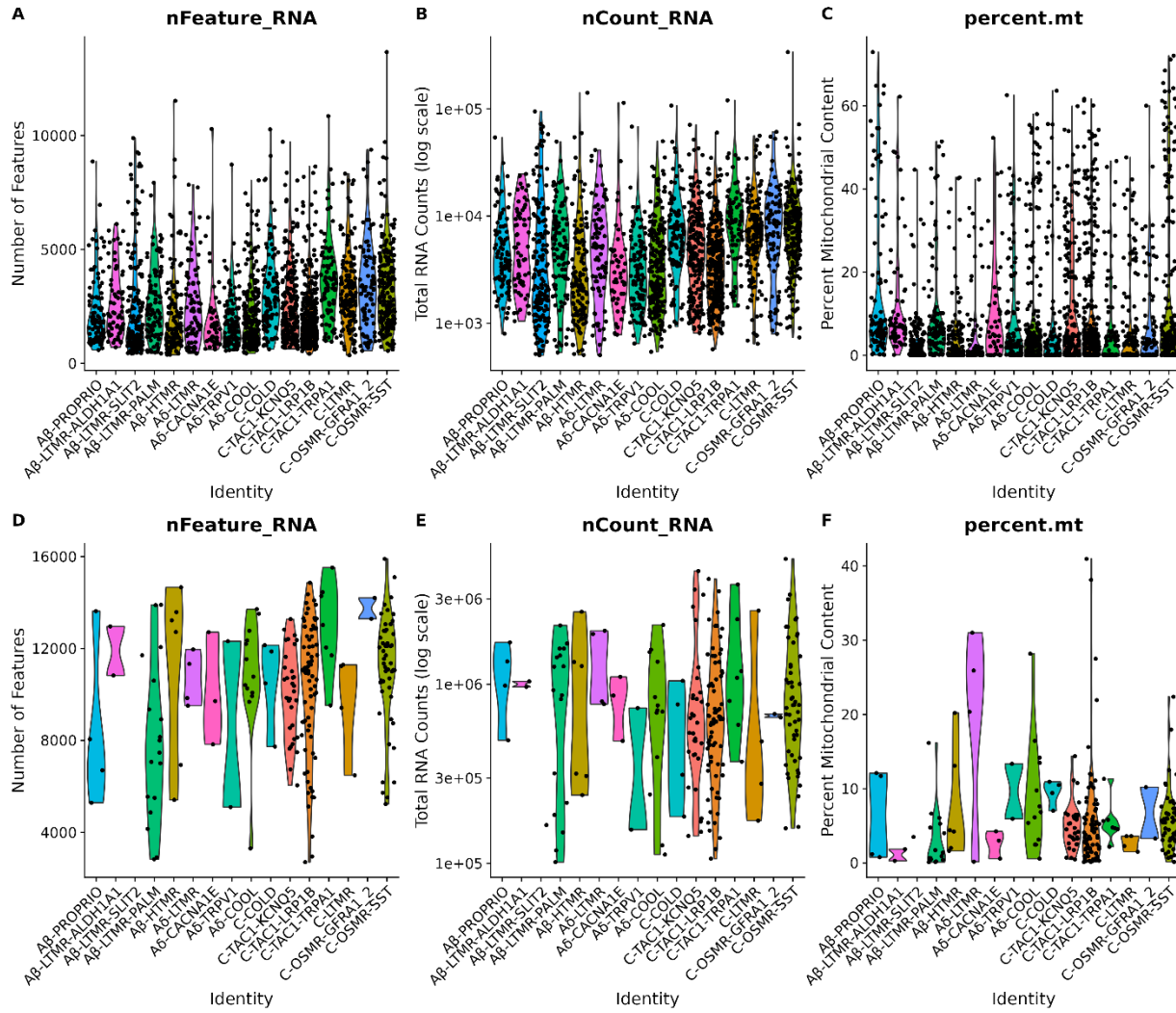
A



1256
1257

Figure S2: Patch-seq whole neuron sampling procedure

1258
1259 Light microscopy time-sequence of one cultured DRG neuron being harvested for Patch-seq following
1260 electrophysiological characterization. Scale bars indicate 50 μ m. Up left to down right: 1) Neuron shown with small
1261 diameter pipette for patch clamp based current clamp recordings. 2) After recording, the recording pipette is
1262 detached, and cytosolic content washed in the pipette tip is transferred to a PCR tube containing lysis buffer. 3) A
1263 second, larger diameter pipette is used for extraction of the entire neuron with neurites. 4) The second pipette is
1264 attached to the neuron using strong negative pressure and the neuron with its neurites is carefully detached and
1265 extracted from the coverslip. 5) Image of the second pipette with the neuron attached shown outside (i.e., above) the
1266 extracellular solution, following which the neuron is carefully placed into the same PCR tube from step 2 containing
1267 lysis buffer. 6) Image of the former position of the neuron, confirming completion of neuronal harvest.



1268

Figure S3: Sequencing metrics of snRNAseq and Patch-seq datasets

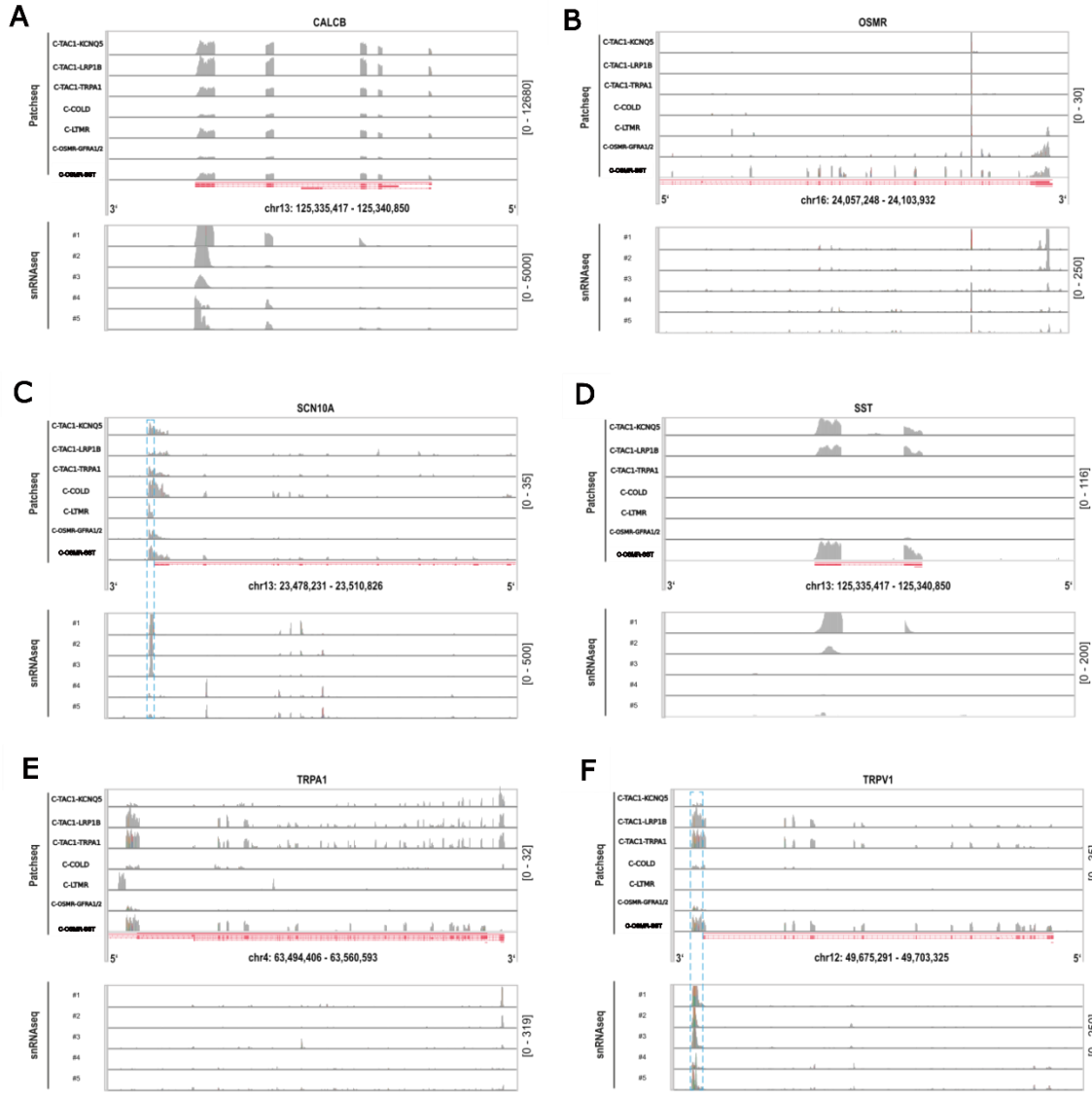
1270

1271

1272

1273

1274



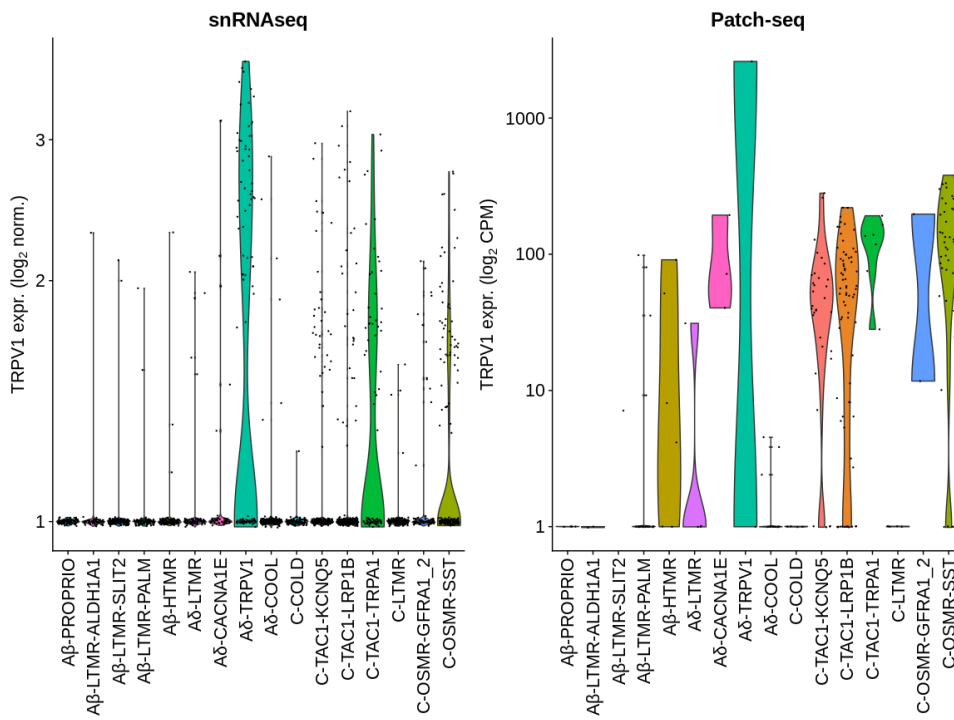
1275

1276 **Figure S4: Illustration of how limitations in porcine reference genome annotation likely**
 1277 **impact gene expression quantification**

1278

1279 **A-F)** Read coverage plots for exemplar genes from Patch-seq (one representative cell per C-fiber type, top) and
 1280 snRNAseq (merged data from multiple cells separated by barcoding reaction, bottom) datasets. X-axis denotes
 1281 genome position (3' and 5' gene ends annotated per gene), and y-axis denotes read coverage (scales shown on right).
 1282 Red track in middle illustrates gene models from pig reference transcriptome annotation (Ensembl 105). Note that
 1283 Smart-seq2 protocol, used for reverse transcriptase for Patch-seq, results in full-length cDNA generation and thus
 1284 more complete coverage of mRNA throughout the whole gene body. In contrast, given our usage of the
 1285 10XGenomics Single Cell 3' Kit, as expected, snRNAseq read coverage are biased towards 3' ends of gene bodies.
 1286 We note that this qualitative inspection revealed that some genes, including SCN10A (c) and TRPV1 (f), show
 1287 some evidence of having several unannotated reads in the 3' UTRs of these genes (highlighted by blue dashed lines),
 1288 which we reason is likely due to incomplete annotation of the 3' UTRs of these genes in the used reference

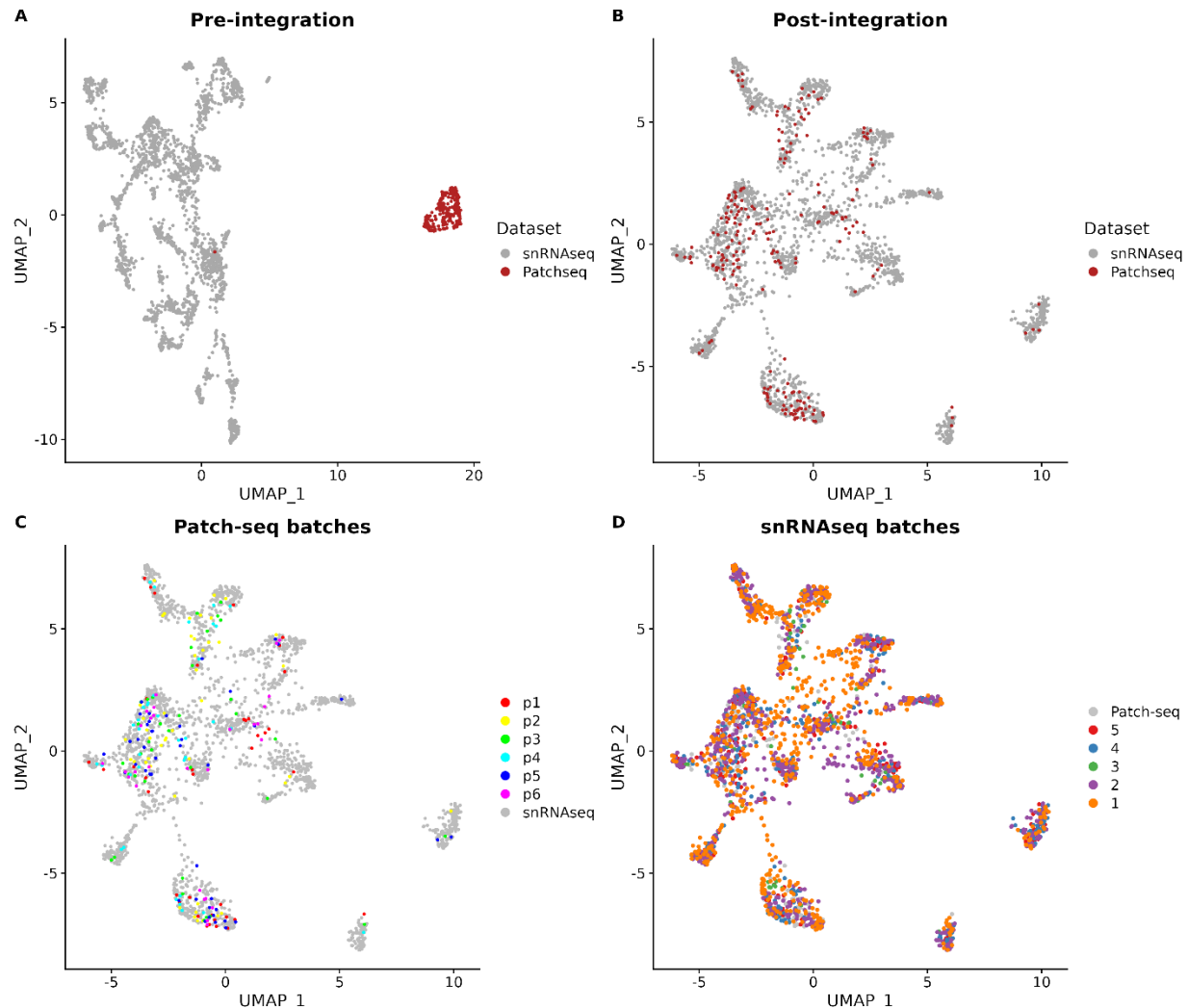
1289 transcriptome. However, this issue appears to be gene specific as the other genes manually assessed, including
1290 CALCB (a), OSMR (b), SST (d) do not appear to qualitatively display evidence of this issue. Note that while 3'
1291 UTR appears well annotated for TRPA1 (e), 5' UTR appears potentially misannotated, as our Patch-seq datasets
1292 showed evidence that some reads were unannotated in these regions.
1293
1294



1295
1296

1297 **Figure S5: TRPV1 expression is consistent between snRNAseq and Patch-seq datasets**

1298 Violin plots showing TRPV1 expression levels across neuronal subtypes in snRNAseq (left) and Patch-seq (right)
1299 datasets. The three clusters with highest TRPV1 expression (A δ -TRPV1, C-TAC1-TRPA1, and C-OSMR-SST) are
1300 consistently identified across both technologies. Y-axis shows normalized expression values (log₂ normalized
1301 counts for snRNAseq; log₂ CPM for Patch-seq). Each dot represents an individual cell/nucleus.

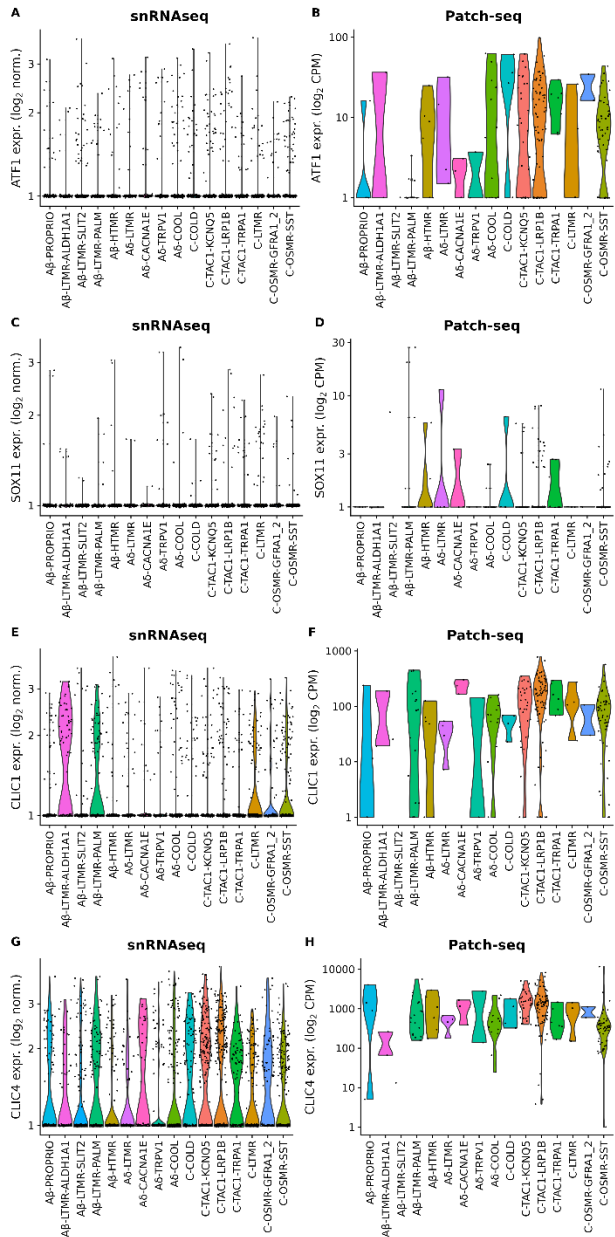


1302

1303 **Figure S6: Integration of snRNAseq and Patch-seq datasets and batch distribution across**
1304 **UMAP space**

1305

1306 UMAP visualizations of single-cell transcriptomics data from pig dorsal root ganglia (DRG) neurons. (A) Pre-
1307 integration view showing separate clusters for snRNAseq (grey) and Patch-seq (red) datasets. (B) Post-integration
1308 view demonstrating successful merging of snRNAseq and Patch-seq data. (C) Integrated data colored by individual
1309 Patch-seq experimental batches (p1-p6), with snRNAseq cells shown in grey. (D) Integrated data colored by
1310 individual snRNAseq animal donors (1-5), with Patch-seq cells shown in grey. Each point represents a single cell or
1311 nucleus.
1312
1313



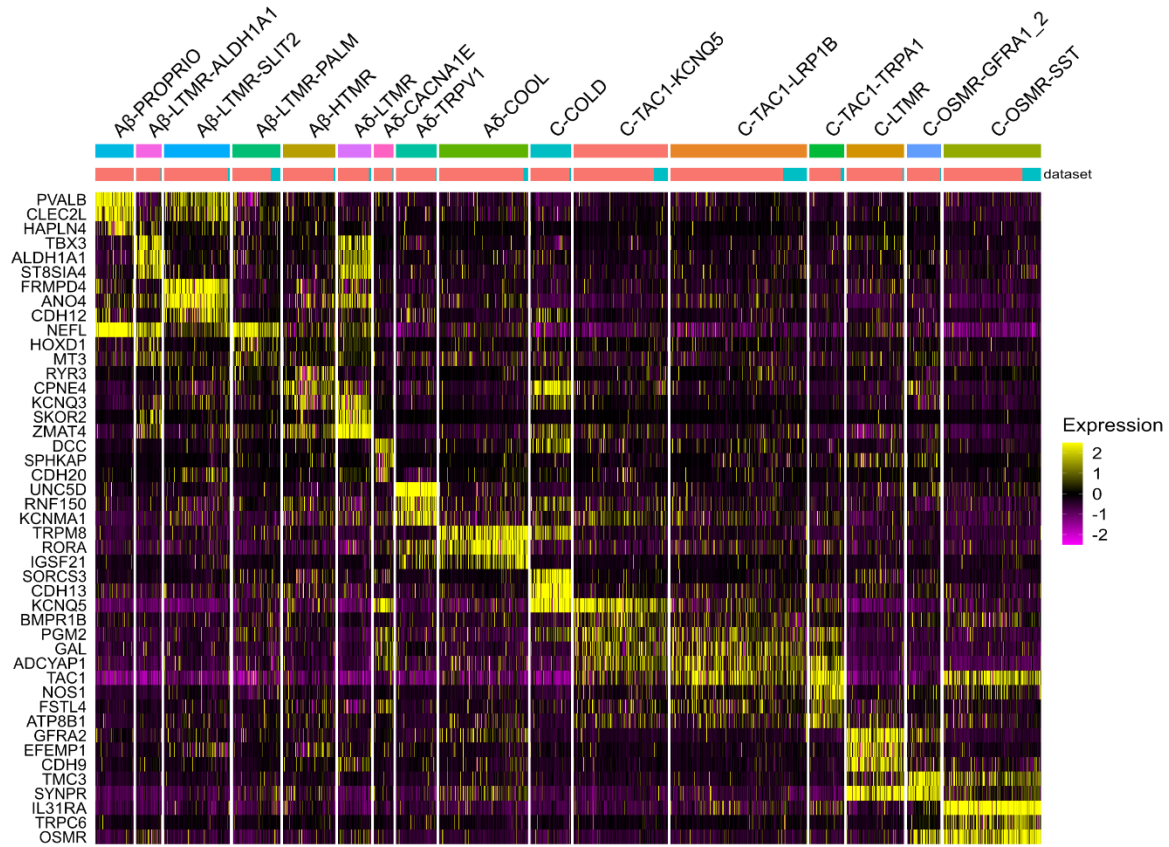
1314

1315 **Figure S7: Comparison of injury-induced and culturing-related gene expression between**
1316 **snRNAseq and Patch-seq datasets.**

(A-D) Expression of known injury-induced genes across neuronal subtypes: ATF1 (A-B) and SOX11 (C-D) in snRNAseq (A, C) and Patch-seq (B, D) datasets. (E-H) Expression of culturing-associated genes: CLIC1 (E-F) and CLIC4 (G-H) in snRNAseq (E, G) and Patch-seq (F, H) datasets. Expression levels shown as log₂-normalized counts (snRNAseq) or log₂ CPM (Patch-seq). Each point represents a single cell/nucleus

1321

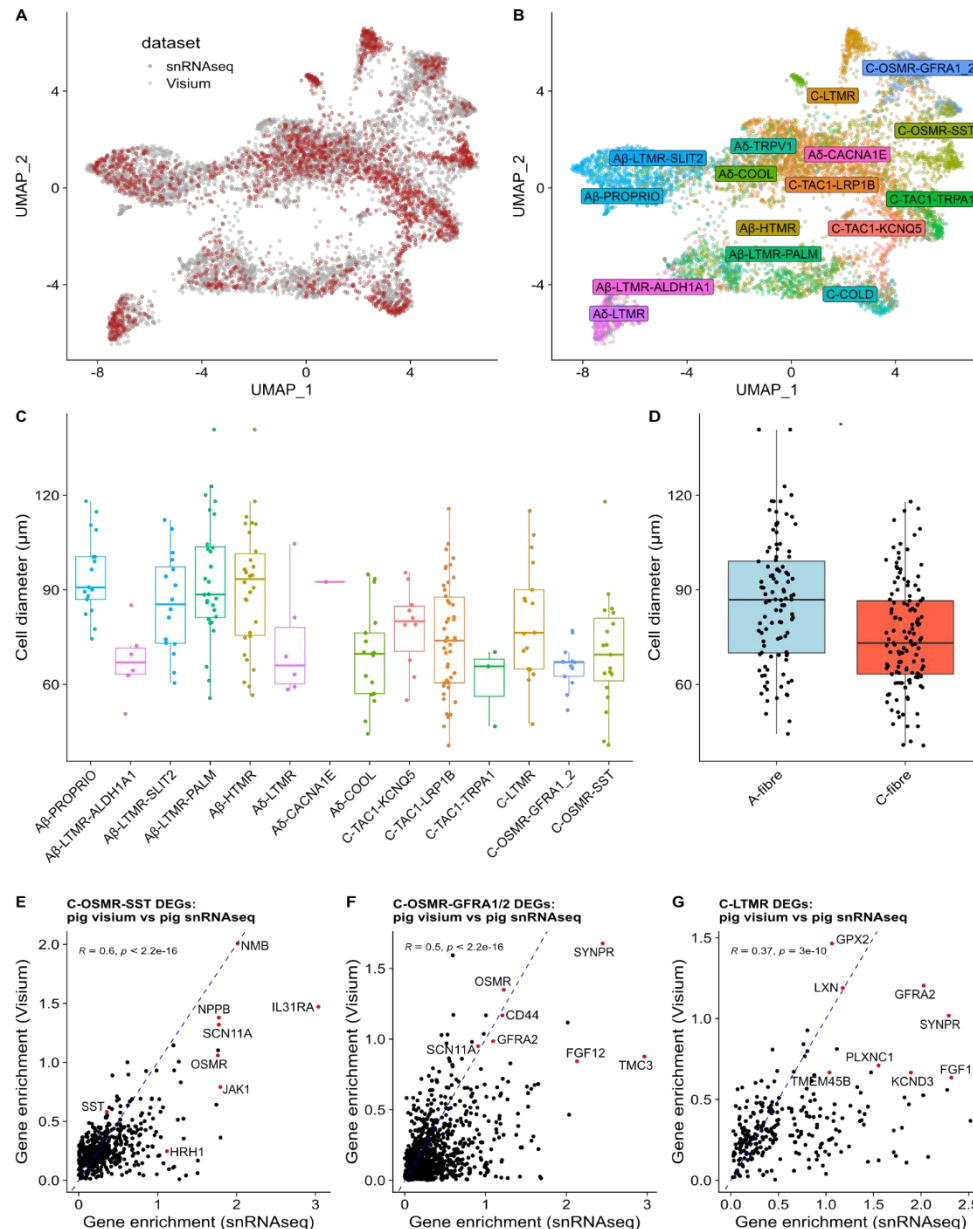
1322



1323

1324 **Figure S8: Expression of marker genes are conserved between Patch-seq and snRNaseq**
1325 **pig datasets**

1326 Heatmap showing the 3 most prominent gene products per neuronal identity. Upper bar indicates neuronal identity.
1327 Lower bar indicates dataset (snRNaseq, red; Patch-seq, blue).
1328



1329

1330

1331 **Figure S9: Spatial transcriptomics of pig DRGs corroborates cell type-enriched marker**
 1332 **gene expression across technologies**

1333 **A)** UMAP representation of integrated gene expression from snRNAseq (red) and Visium-based spatial
 1334 transcriptomics (grey). **B)** Same representation as in (A), but with colours distinguishing the mapped cell types.
 1335 **C,D)** Cell diameters based on manual quantification of 230 DRG neurons from the Visium dataset illustrated as
 1336 neuronal subtype (c), and at broad cell type resolution ($85.5 \pm 1.9 \mu\text{m}$ for A-fibers, $73.7 \pm 1.6 \mu\text{m}$ for C-fibers,
 1337 $t=4.81, df=226.72$, Welch's t-test $p\text{-value} = 2.72 \times 10^{-6}$, mean \pm SEM) (d). **E-G)** Illustration of concordance of cell
 1338 type-enriched differential gene expression (DEGs) for C-OSMR-SST (E), C-OSMR-GFRA1/2 (F), and C-LTMR
 1339 cells (G). Each dot reflects a gene, with x- and y-axis values indicating \log_2 fold changes of enrichment of target cell
 1340 type (e.g., C-OSMR-SST cells) compared to all other cells in snRNAseq dataset (x-axis) and Visium spatial
 1341 transcriptomics dataset (y-axis). Genes subset to those with positive enriched expression in both technologies. Inset
 1342

1343 values indicate Pearson correlations (R) and associated p-values. Genes denoted in red indicate cell type markers or
1344 otherwise notable genes.
1345

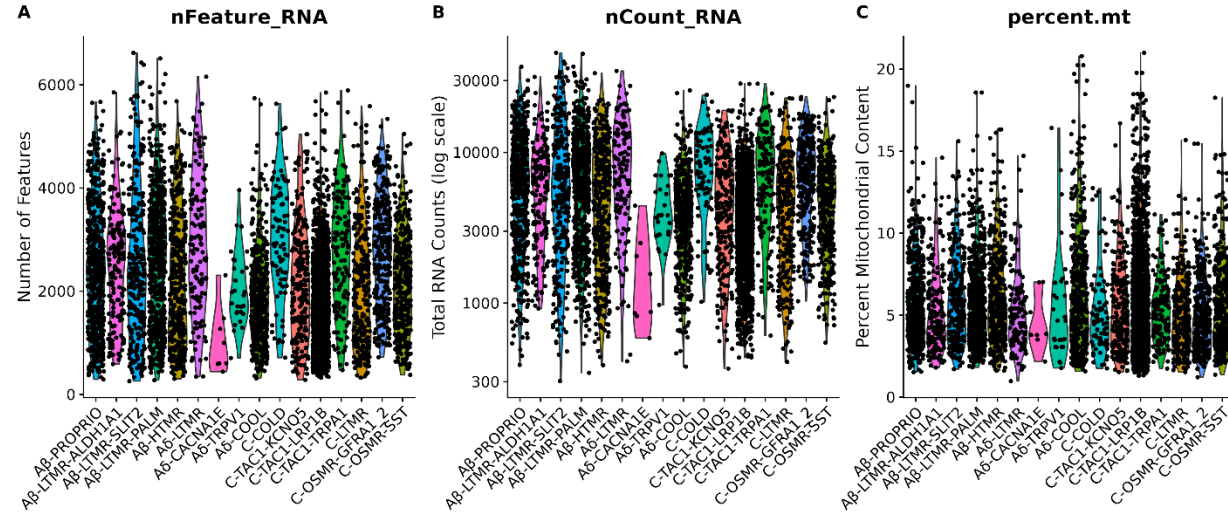


Figure S10: Sequencing metrics Visium data

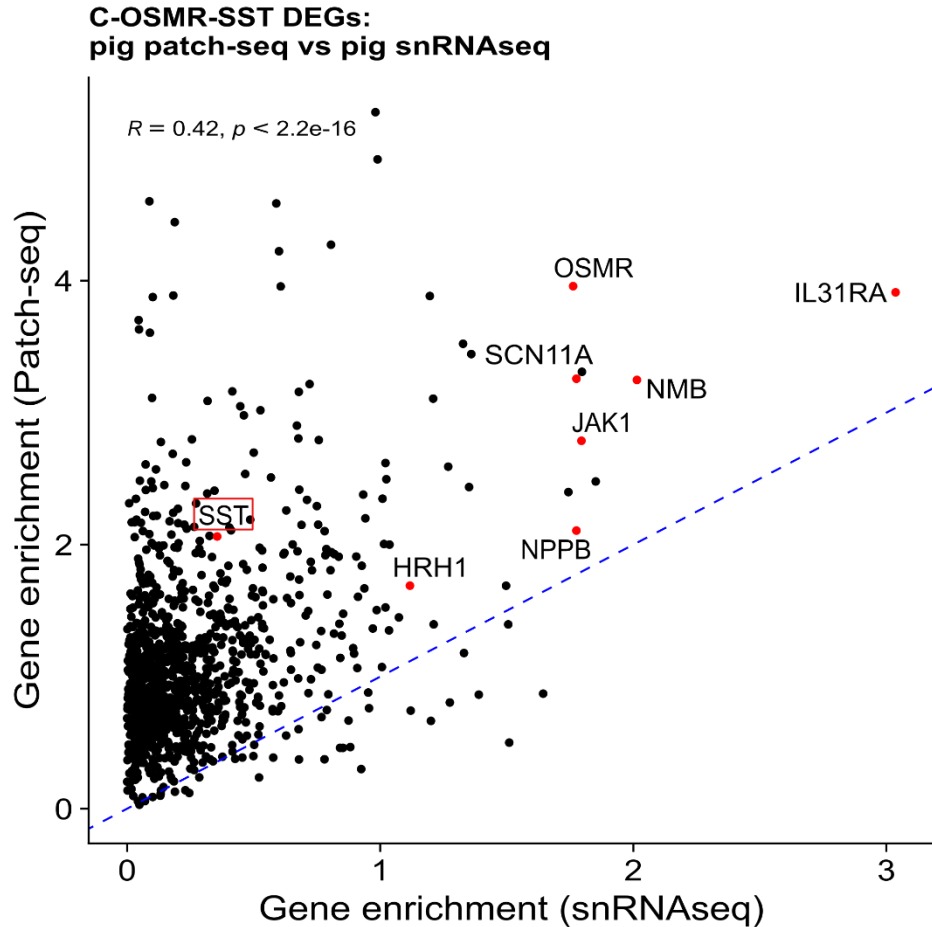
1346

1347

1348

1349

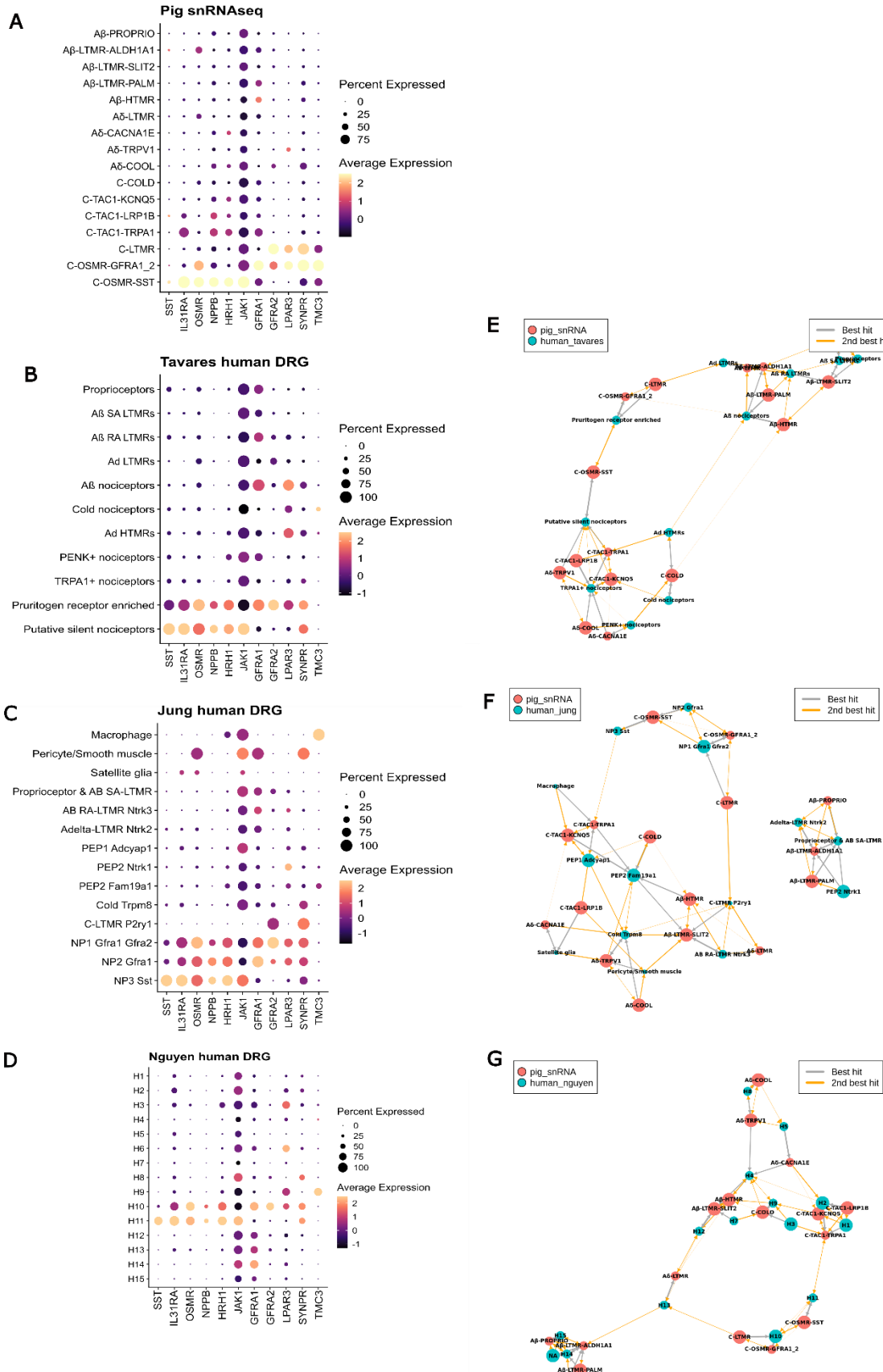
A-C) Sequencing metrics for pig Visium dataset: a) number of reads per cell, b) number of genes per cell and c) fraction of mitochondrial reads per assigned neuronal identity. Each data point represents an individual cell.



1351

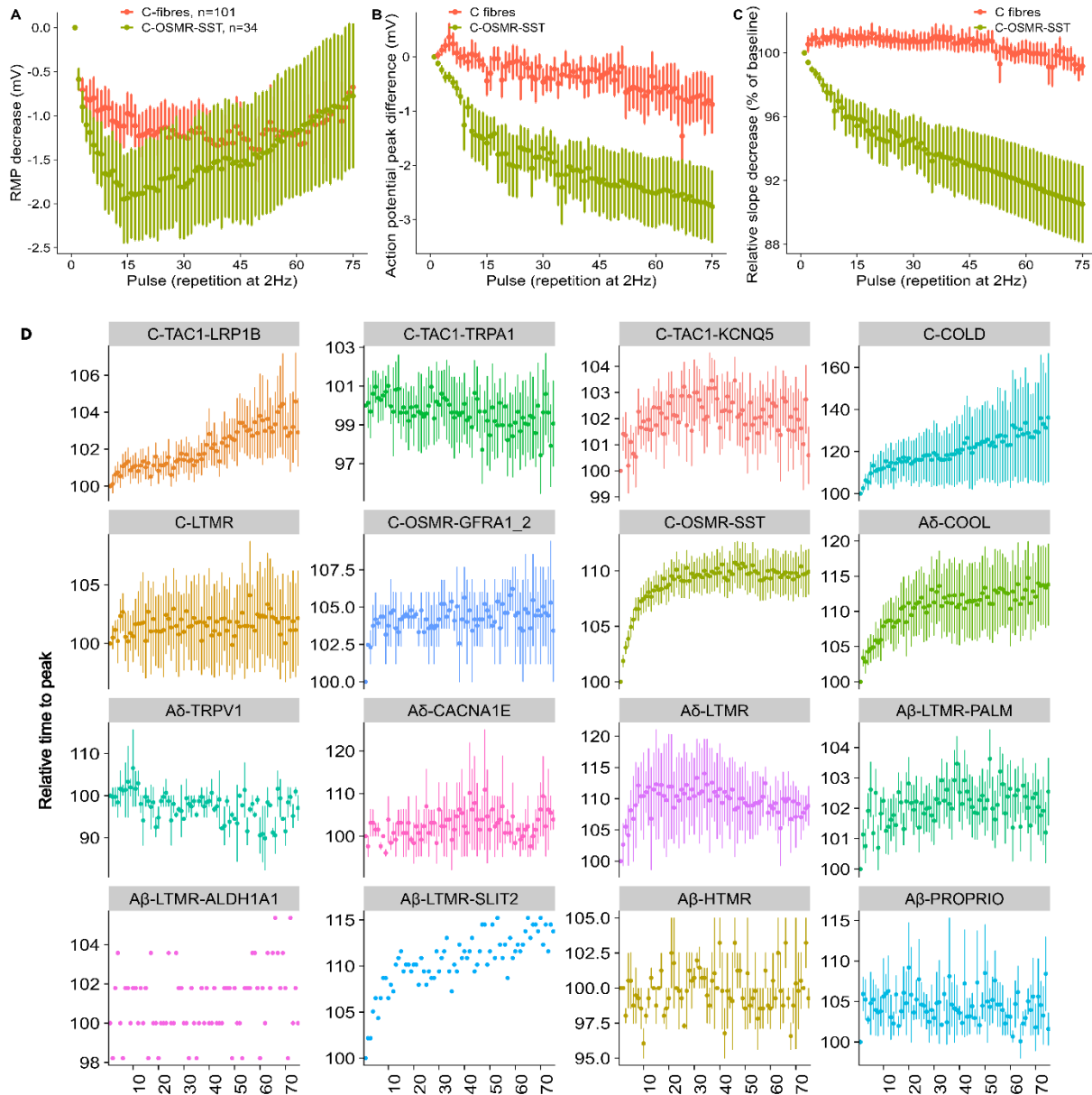
1352 **Figure S11: Concordance of differentially expressed genes in C-OSMR-SST across Patch-**
1353 **seq and snRNAseq**

1354
1355 Concordance of differentially expressed genes (DEGs) in C-OSMR-SST cells across Patch-seq and snRNAseq
1356 datasets. Each point represents a gene, with the x-axis indicating gene enrichment log₂ fold change in the snRNAseq
1357 dataset and the y-axis showing the same in the Patch-seq dataset, both derived from pig samples. Only genes with
1358 positive enrichment in both datasets are shown. Inset values indicate the Pearson correlation coefficient (R) and
1359 associated p-value. Genes denoted in red indicate cell type markers with SST highlighted despite relatively lower
1360 expression in the snRNAseq dataset.
1361



1363 **Figure S12: Pig and human DRG transcriptomic cell-type replicability**

1364 **A-D)** Dotplots showing expression of key marker genes for C-OSMR-SST neurons and related cell types across
1365 different datasets. The size of each dot represents the percentage of cells expressing the gene, while the color
1366 intensity indicates the average expression level. **(A)** Pig snRNAseq data collected in this study. **(B-D)** Human DRG
1367 data subsets from previously published cross-species atlas: **(B)** Tavares et al. human DRG dataset, **(C)** Jung et al.
1368 human DRG dataset, and **(D)** Nguyen et al. human DRG dataset. **E-G)** MetaNeighbor cluster graphs comparing pig
1369 snRNAseq cell types (red nodes) to human DRG cell types (blue nodes) from different studies in the cross-species
1370 atlas. **(E)** Comparison with Tavares et al. human DRG data. **(F)** Comparison with Jung et al. human DRG data. **(G)**
1371 Comparison with Nguyen et al. human DRG data.
1372



1373

1374

Figure S13: Extended electrophysiological characterization of CMi-fibers

1375

1376

Supplemental Data on functional biomarkers derived from *in vivo* microneurography experiments. **A**) Relative change in maximum action potential slope upon 75 rectangular 1000 pA stimulations with 10 ms and 2 Hz for C-OSMR-SST cells compared to all other Patch-seq characterized C-fiber neurons (mean change 0.906 ± 0.0235 SEM vs. 0.992 ± 0.00586 SEM; Mann-Whitney U = 2829.5, $p < 1.733^{-08}$). **B**) Relative change in maximum action potential peak voltage upon 75 rectangular 1000 pA stimulations with 10 ms and 2 Hz for C-OSMR-SST cells compared to all other C-fiber neurons (mean change -3.08 ± 0.723 mV vs. -0.877 ± 0.540 mV; Mann-Whitney U = 2589.5, $p < 9.855 \times 10^{-06}$). **C**) Relative change in resting membrane potential upon 75 rectangular 1000 pA stimulations with 10 ms and 2 Hz for C-OSMR-SST cells compared to all other C-fiber neurons. **D**) Relative time to peak during 75 rectangular 1000 pA stimulations with 10 ms and 2 Hz for all cell types in the dataset. Error bars indicate SEM.

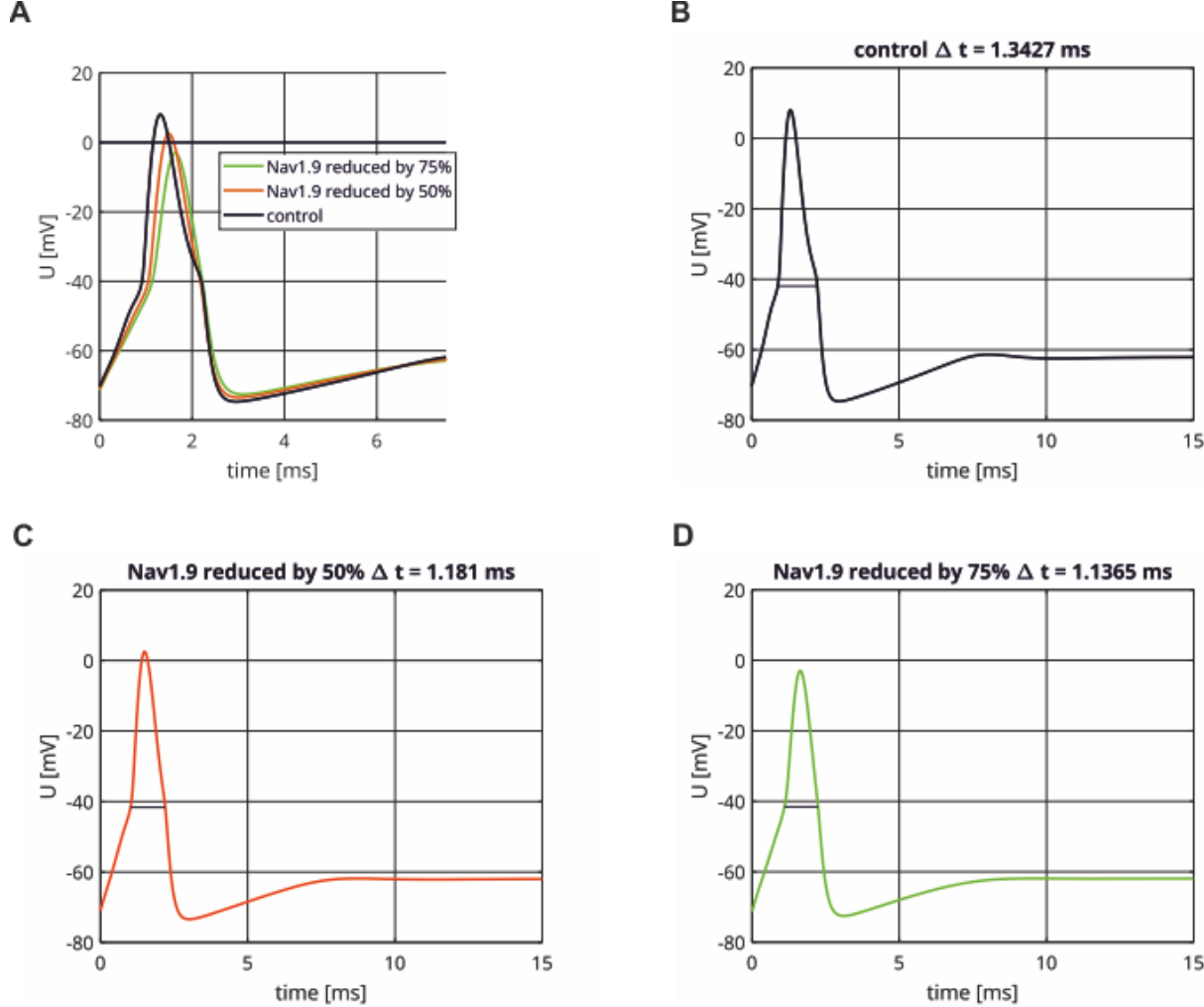
1385

1386

1387

1388

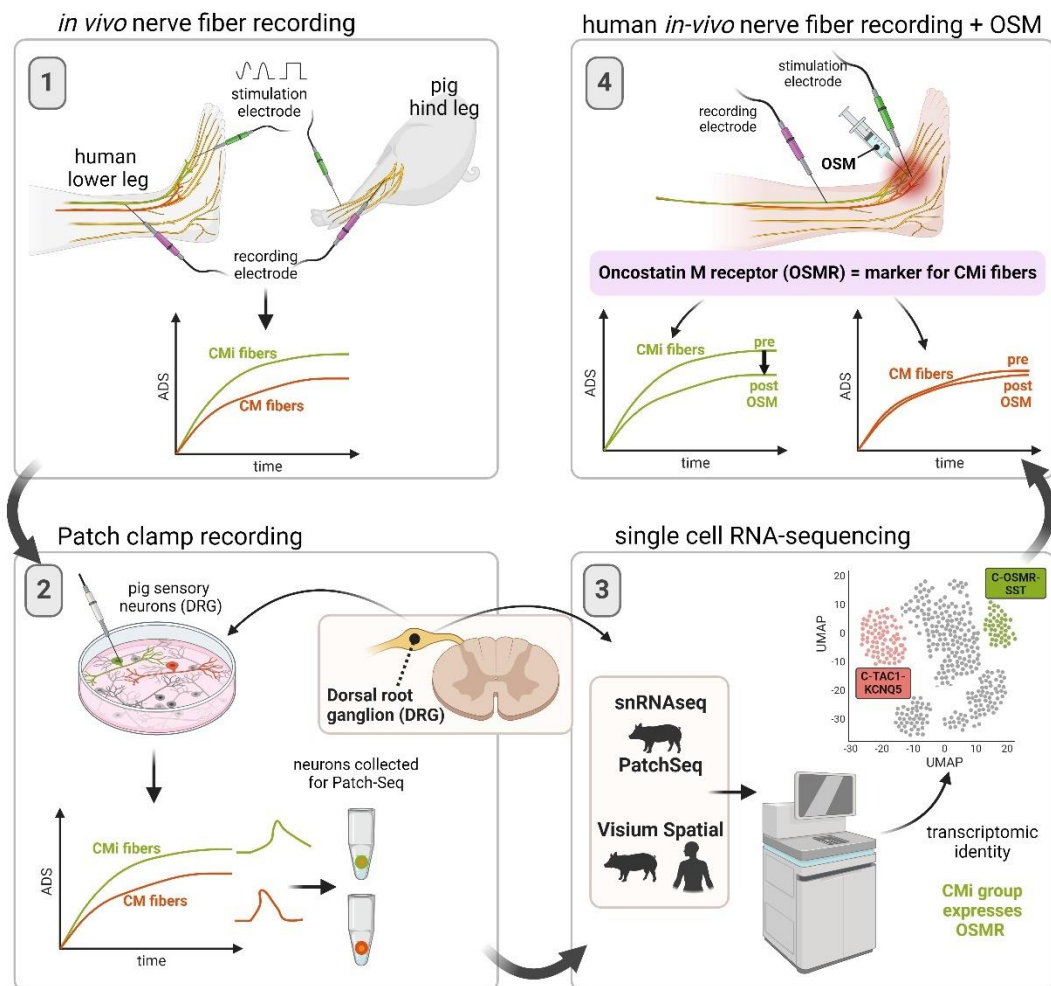
1389 **Figure S14: Simulated impact of SCN11A abundance on the AP morphology in C-OSMR-
1390 SST neurons**



1391
1392 **(A):** Overlay of the three simulated AP with the relative abundance of SCN isoforms corresponding to their gene
1393 expression **B:** The black line (control) shows the simulated AP with the relative abundance of SCN isoforms
1394 corresponding to their gene expression. The maximal conductance attributed to SCN11A is stepwisely reduced to
1395 50% (**C**) (red line) and 75% (**D**) compared to the control. The maximal conductances attributed to the
1396 other isoforms are increased proportionally to their expression, such that the total maximal sodium conductance
1397 remains unchanged. At the beginning of the simulation the neurons are in their resting state. The AP width (Δt) is
1398 measured at the threshold voltage and indicated by a horizontal line. Current injection starts at time 0 and lasts until
1399 the end of the simulation period. Maximal slopes: **A:** 213.2 mV/ms, **B:** 152.3 mV/ms. **C:** 109.6 mV/ms.

1400

1401 **Figure S15: Graphical Abstract**



1418 **Supplementary Table 1**

1419 Overview on identified fiber classes with assumed function, corresponding fiber classes, electrophysiological
 1420 markers, gene expression markers, and correspondence and MetaNeighbor-based match type and score to
 1421 harmonized cross-species atlas. Reciprocal top hit indicates cell type pair is best matching cell type based on bi-
 1422 directional taxonomy comparison.

Subgroup name	Assumed function	Corresponding fiber class (inferred)	Ephys Markers	Gene expression markers	Corresponding cell type in cross species atlas	Cross-species match type (AUC)
C-TAC1-KCNQ5	nociception (specification unclear)	Polymodal nociceptors	High AP-Amplitude and Maximum	KCNQ5, TAC1, CALCB, ADCYAP1, NTRK1, SCN10A	Calca+SST R2	Reciprocal_top_hit (0.88)
C-TAC1-LRP1b	nociception (specification unclear)	Polymodal nociceptors	High AP-Amplitude and Maximum	LRP1b, TAC1, CALCB, ADCYAP1, NTRK1, SCN10A	Calca+SST R2	Hit_above_0.7 (0.87)
C-TAC1-TRPA1	nociception (specification unclear)	Polymodal nociceptors	High AP-Amplitude and Maximum	TRPA1, TAC1, CALCB, ADCYAP1, NTRK1, SCN10A	Calca+Oprk1	Hit_above_0.7 (0.84)
C-LTMR	social touch (?)	C-touch	Low max Slope	PIEZO2, CDH9, GFRA2, FGF12, SYNPR	Th	Reciprocal_top_hit (0.96)
C-OSMR-SST	Cmi, fibers, itch, neuro-immune modulation	histamine sensitive mechano-insensitive ("silent") C-nociceptors /all silent nociceptors ?	Low FF, High Sinus, High ADS, Long APD	SST, IL31RA, OSMR, HRH1, JAK1, NPPB, SCN11A	SST	Reciprocal_top_hit (0.96)
C-OSMR-GFRA1/2	nociception		n=2, no statement possible	PIEZO2 high, SYNPR, GFRA1, GFRA2,	Mrgprd	Reciprocal_top_hit (0.94)

				PLCB3, TMC3		
C-COLD	noxious cold detection	C-cold nociceptors	Compared to Cool: Long APD, higher AP max, dep TH, less max slope but more pronounced Overshoot	TRPM8, KIT, SCN9A, SCN10A, SCN11A	Calca+Smr 2	Reciprocal _top_hit (0.78)
A δ -LTMR	mechanosensation		No specific Ephys Marker	PIEZO2, NTRK2, BAIAP2L1, PCDH7, KCNQ3, SCN1/2/8/9A	Ntrk3low+ Ntrk2	Reciprocal _top_hit (0.94)
A δ -CACNA1E	nociception		Most dep TH among Adeltas	SCN9-10A, B4GALT6, DCC, CREB5, CACNA1E, NTRK2	Calca+Dcn	Reciprocal _top_hit (0.93)
A δ -COOL	non-noxious cold detection	A δ - cold detection fibers	short APD, low AP max + AMP, Hyperpol TH, low max Overshoot, highest fraction of spontaneous activity	TRPM8, FOXP2, RORA, SCN2/8/9A	Trpm8	Reciprocal _top_hit (0.92)
A δ -TRPV1	nociception (specification unclear)	Adelta-TRPV1high	n=2, no statement possible	SCN9A, TRPV1, ZNF521, UNC5D	Rxfp1	Reciprocal _top_hit (0.92)
A β -LTMR-PALM	mechanosensation		Seem functionally heterogenous, highest SD in almost all features, functional subgroups?	PALM, PIEZO2	Ntrk3high+ S100a16	Hit_above_0.7 (0.85)
A β -LTMR-ALDH1A1	mechanosensation		n=3, lower AP amplitude + AP max than other AB LTMRs, highest FF among AB LTMRs	ALDH1A1, PIEZO2	Ntrk3high+ Ntrk2	Hit_above_0.7 (0.93)

A β -LTMR-SLIT2	mechanosenstation		No specific functional marker	SLIT2, PIEZO2	Pvalb	Reciprocal_top_hit (0.96)
A β -HTMR	nociception		Highest max. slope of A β mechanoceptors	PIEZO2, CPNE4, PLXNA2, SCN8-10A	Ntrk3high+ S100a16	Hit_above_0.7 (0.79)
A β -Proprio	proprioception	A-proprioceptors	Hyperpol. TH and RMP, AHP, highest max. subthreshold slope	PVALB, SPP1, ETV1	Ntrk3high+ Ntrk2	Reciprocal_top_hit (0.94)

1423
1424

1425
1426